# Polariton-Polariton Coherent Coupling in a Molecular Spin-Superconductor Chip

Carolina del Río,[1] Marcos Rubín-Osanz,[1] David Rodriguez,[2] Sebastián Roca-Jerat,[1] María Carmen Pallarés,[1,3] J. Alejandro de Sousa,[4] Paweł Pakulski,[5] José Luis García Palacios,[1] Daniel Granados,[6] Dawid Pinkowicz,[5] Núria Crivillers,[4] Anabel Lostao,[1,3,7] David Zueco,[1] Alicia Gomez,[2] and Fernando Luis[1,*]

[1]*Instituto de Nanociencia y Materiales de Aragón (INMA), CSIC, Universidad de Zaragoza, 50009, Zaragoza, Spain*
[2]*Centro de Astrobiología (CAB), CSIC-INTA, 28850 Torrejón de Ardoz, Madrid, Spain*
[3]*Laboratorio de Microscopias Avanzadas (LMA), Universidad de Zaragoza, 50018 Zaragoza, Spain*
[4]*Institut de Ciència de Materials de Barcelona (ICMAB-CSIC), Carrer dels Til.lers, 08193 Cerdanyola del Vallès, Spain*
[5]*Jagiellonian University, Faculty of Chemistry, Krakow, Poland*
[6]*IMDEA-Nanoscience, Cantoblanco, 28049 Madrid, Spain*
[7]*Fundación ARAID, 50018 Zaragoza, Spain*

(Received 10 March 2026; revised 22 June 2026; accepted 2 October 2026; published 25 November 2026)

The ability to establish coherent communication channels is key for scaling up quantum devices. Here, we engineer interactions between distant polaritons, hybrid spin-photon excitations formed at different lumped-element superconducting resonators within a chip. The chip consists of several resonator pairs, slightly detuned in frequency to make them addressable, capacitively coupled within each pair and inductively coupled to a common readout line. They interact locally with samples of PTMr and Tripak$^-$ organic free radicals, deposited onto their inductors, which provide model $S = 1/2$, $g \simeq 2$ spin ensembles. Frequency-dependent microwave transmission experiments, performed at very low temperatures, measure polariton frequencies as a function of magnetic field in different scenarios. When only one resonator within a pair hosts a molecular sample, the results evidence that spins couple remotely to the empty LER as well as to the local cavity mode. If both resonators interact with a spin ensemble, the magnetic field tunes the polariton frequencies relative to each other, on account of the different spin-photon interactions at each LER. When polaritons are brought into mutual resonance, the microwave transmission spectroscopically resolves an avoided level crossing that evidences a polariton-polariton interaction mediated by the circuit. Then, pump-probe experiments reveal that the excitation of a polariton within a connected pair is indeed felt, thus it can be read out, by the other one. Model calculations, compatible with the experimental parameters and results, suggest that the system excitation eigenstates show photon-photon and spin-spin correlations and entanglement near the polariton-polariton anticrossing.

DOI: 10.1103/xvjl-h44h

## I. INTRODUCTION

Circuit quantum electrodynamics (circuit QED) studies quantum matter interacting with photon modes of superconducting cavities [1,2]. Besides the fundamental interest of accessing strong [3] and ultra-strong [4] light-matter interaction regimes, circuit QED also provides a platform for reading out solid-state qubits [5], for generating [6] and storing [7] quantum states of light and for quantum sensing [8], among others. In addition, cavity photons mediate effective interactions between qubits coupled to the same cavity, which can be exploited for scaling up quantum computing architectures [9]. Such a quantum bus has been realized with superconducting qubits [10,11] and with spin qubits in semiconductors [12–14], both of which couple to the electric photon field.

The magnetic spin-photon interaction is much weaker, but it is enhanced for macroscopic spin ensembles [15–30]. This has allowed coupling collective spin excitations from NV$^-$ centers in a diamond crystal to a superconducting qubit [31], and also coupling two distant magnetic samples, either NV$^-$s [32] or organic free radicals [33], through a coplanar superconducting resonator. The need of coupling both ensembles to the same cavity mode adds, however, some constraints. For instance, they must be located at specific positions determined by the photon magnetic field profile. Besides, the symmetry of the resulting coupled

*Contact author: fluis@unizar.es

*Published by the American Physical Society under the terms of the Creative Commons Attribution 4.0 International license. Further distribution of this work must maintain attribution to the author(s) and the published article's title, journal citation, and DOI.*

states hinders a direct determination of the circuit mediated interaction by standard spectroscopic measurements [32].

In this work, we move beyond these limitations and explore a modular hybrid quantum platform, in which distant polaritons, i.e., light-matter hybrid states generated by local spin-photon interactions at different lumped-element superconducting cavities, can be tuned by a magnetic field, addressed *in situ* in a multiplexable manner and mutually coupled. We study two different scenarios, with either one or two molecular spin ensembles interacting with a resonator pair. We also perform pump-probe experiments that exploit one polariton to sense the excitation of the other one. The results, supported by theoretical simulations, suggest that this scheme offers the possibility of generating, tuning and detecting excitations that simultaneously involve correlations between distant spins *and* microwave cavity photons. It also offers a high design flexibility, e.g., to build in asymmetries that render each polariton distinguishable from the others. Besides, it is inherently scalable to multiple nodes, which would make it relevant for applications of molecular spin qubits and qudits [34–40] to quantum simulation [41–43] and quantum computing [44,45].

## II. EXPERIMENTAL SETUP

### A. Superconducting circuits

The device used in this work is sketched in Figs. 1(a) and 1(b) and described in detail in Appendix A 1. The chip consists of 7 pairs of superconducting lumped-element *LC* resonators (LERs), all coupled to the same readout line [29,30]. They are fabricated by maskless optical lithography on a 125 nm thick NbTiN film deposited by sputtering onto a silicon wafer. The relevant properties of each superconducting LER, i.e., its resonance frequency $\omega_{\mathrm{r},i}$ and the photon loss rate $\kappa_i$ $(i = 1, \ldots, 14)$, can be tailored within wide ranges without affecting the transmission properties of the device. In the chip of Fig. 1(a), different $\omega_{\mathrm{r},i}/2\pi$ ranging from 1.7 to 3.3 GHz were tuned by varying the capacitor geometries while leaving all inductors, which provide the coupling to the spin samples, the same. This allows multiplexing the LER readout, as shown in Appendixes A 1 and A4.

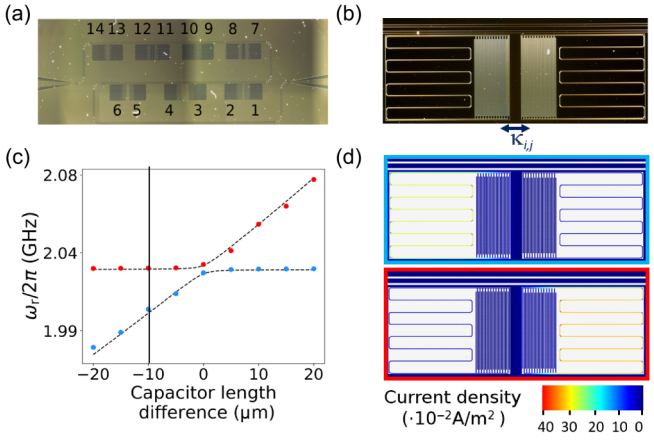


FIG. 1. (a) Image of a bare chip (without spins) hosting seven superconducting LER pairs coupled to a common transmission line. (b) Optical microscopy image of a capacitively coupled LER pair. (c) Resonance frequencies of a LER pair calculated as a function of the difference between their finger capacitor lengths. The coupling $\kappa_{i,j}$ introduces a mode splitting $\Delta\omega_{\mathrm{r}} = 2\kappa_{i,j}$ when the two LERs are identical. (d) Simulations of the single-photon current density, which generates the photon magnetic field, for the two resonant modes of a detuned LER pair [vertical line in (c)].

The two LERs within each pair are capacitively coupled, with a coupling strength $\kappa_{i,j}$ that is controlled by the separation between their respective capacitors. If they were identical, this coupling would lead to an avoided level crossing, shown in Fig. 1(c), with a frequency splitting $\Delta\omega_{\mathrm{r}} = 2\kappa_{i,j}$ [46] between symmetric and antisymmetric modes delocalized all over the LER pair (Fig. 7 in Appendix A 1). Here, we detune the "bare" resonance frequencies $\omega_{\mathrm{r},i}$ and $\omega_{\mathrm{r},j}$ of the two LERs by making the lengths of their interdigitated capacitors different. The effect that the capacitive coupling has on the mode frequencies and states then depends on the ratio of $\kappa_{i,j}$ to the frequency detuning. When $|\omega_{\mathrm{r},i} - \omega_{\mathrm{r},j}| > \kappa_{i,j}$, the photon magnetic field becomes predominantly localized at either one or the other LER [Fig. 1(d) and Appendix A 1]. This sort of "dispersive" condition ensures that, in spite of their mutual coupling, each LER can still be addressed by choosing the appropriate frequency.

### B. Synthesis, characterization and integration of model spin ensembles

These LERs can host samples of two different organic free-radical molecules. The molecular structures of perchlorotriphenylmethyl (PTMr) and benzo[1, 2-*c*:3, 4-*c*′:5, 6-*c*″]tris([1, 2, 5]thiadiazole)2, 2, 5, 5, 8, 8-hexaoxide (Tripak$^-$) radicals, synthesized by following chemical procedures reported elsewhere [47,49], are shown in Figs. 2(a) and 2(b). These molecules show quite long spin coherence times [47,48] and can be easily integrated in devices from solution. They were dropped onto the LER inductors and then left dry in the dark (see Appendix A 2 for details). The solution contained also a polystyrene polymer that prevents agglomeration of the radical molecules in the dry deposits. Each of these deposits is then highly stable at ambient conditions and provides a model ensemble of $N \sim 5 \times 10^{12} - 5 \times 10^{14}$ identical $S = 1/2$ spins with a quasi-isotropic $g$ factor, very close to that of a single electron. The latter property leads, at any magnetic field $B$ and despite the random molecular orientations, to a well-defined narrow spin resonance. This was characterized as a function of $B$ by coupling the molecules to a

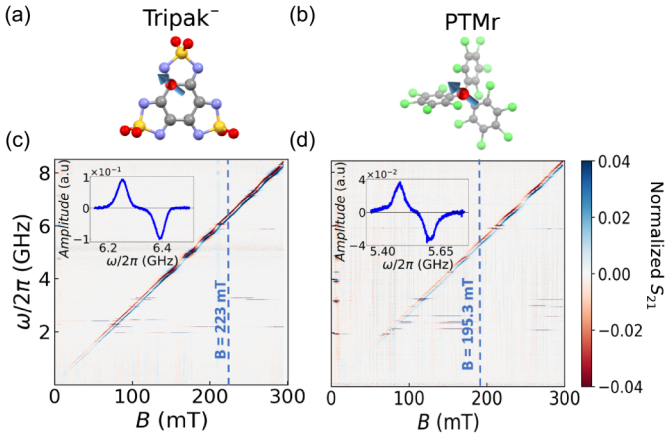


FIG. 2. Molecular structures of the organic free radical molecules used in this study: (a) Tripak$^-$ [47]; (b) PTMr [48]. Here, carbon atoms are represented in gray, chlorine atoms in green, nitrogen atoms in blue, sulfur atoms in yellow and oxygen atoms in red. (c),(d) Broadband microwave absorption spectra of Tripak$^-$ and PTMr, respectively, measured at $T = 11$ mK by coupling them to a superconducting waveguide. The insets show normalized transmission data measured at the magnetic fields indicated by vertical dashed lines.

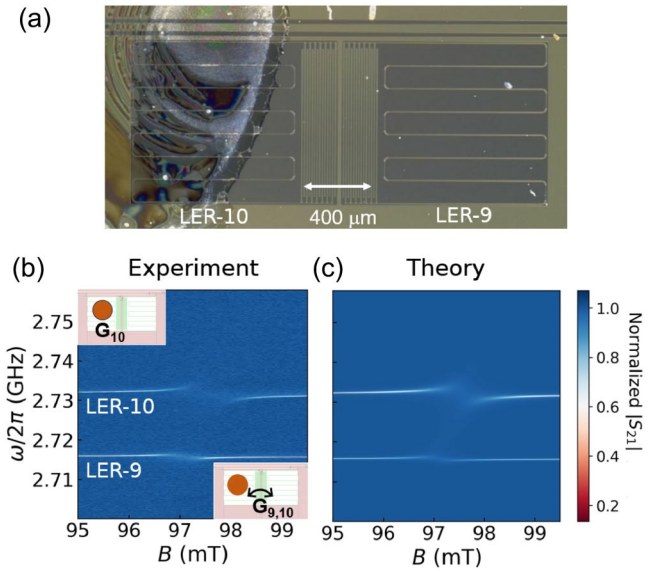


FIG. 3. (a) Optical microscopy image of a $N \sim 5 \times 10^{12}$ PTMr free radical deposit on the inductor of LER-10, forming a coupled pair with LER-9, which remains empty. (b) Color plot of the normalized transmission amplitude $|S_{21}|$ measured, at $T = 11$ mK and for a $-95$ dBm input power (equivalent to a photon number $n \sim 6.8 \times 10^5$ for LER-9 and $n \sim 8.1 \times 10^5$ for LER-10), near the resonance frequencies of the two LERs. The data show a detectable coupling of the spins to both resonant modes, being $G_{10}/2\pi = 5.4$ MHz the coupling strength to the "local" LER-10 and $G_{9,10}/2\pi = 2.5$ MHz the remote interaction with LER-9. (c) Theoretical calculation of the microwave transmission obtained from Eq. (1) by using input-output theory (Appendixes D 2 and D 3), for $G_{10}/2\pi = 5.4$ MHz and $\kappa_{9,10}/2\pi = 6.5$ MHz.

superconducting waveguide. Representative broadband spectroscopy results, measured at very low temperatures and normalized as described in [50,51], are shown in Figs. 2(c) and 2(d). Additional data are shown in Fig. 10 in Appendix A 2. The spin resonance frequency $\Omega_S$ increases linearly with $B$, as expected for a paramagnetic system. The slightly different slopes reveal different $g$ factors, 2.001 for PTMr and 2.003 for Tripak$^-$. The resonance line shape, shown in the insets of Fig. 2, allows estimating the spin linewidth $\gamma/2\pi \simeq 7$–$12$ MHz for both samples, depending on concentration.

## III. RESULTS

### A. One spin ensemble coupled to a LER pair: Remote spin photon coupling

We now consider the response of the hybrid LER-spin units. The first situation is shown in Fig. 3(a): only one of the LERs, LER-10, hosts a sample of $N \sim 5 \times 10^{12}$ PTMr molecules, while the second one, LER-9, remains empty. With this setup, we aim to compare the couplings of the same spin ensemble to local and remote photon modes.

Microwave transmission data $S_{21}$ were measured at very low temperature as a function of frequency and magnetic field, and for different input powers, using the setup and conditions described in Appendixes A 3 and A 4. In the figures that follow, we plot the transmission amplitude $|S_{21}|$ normalized by its maximum value within the relevant experimental range. Results for LER-9 and LER-10 are shown in Fig. 3(b). The two resonant modes lead to horizontal lines of reduced transmission at slightly different frequencies. The resonance visibility is then defined as the normalized transmission dip amplitude. When the magnetic field brings $\Omega_S$ close to the frequency of their host, LER-10, the mode shifts, broadens and its visibility decreases. These features characterize the local spin-photon coupling. Fitting these data using input-output theory (as described in Appendixes D 2 and D 3) gives a collective spin-photon coupling strength $G_{10}/2\pi = 5.4$ MHz, and spin and photon linewidths $\gamma = 7.3$ MHz and $\kappa_{10} = 44$ kHz, respectively, which correspond to high cooperativity $C_{10} \equiv G_{10}^2/\kappa_{10}\gamma \sim 91$.

Interestingly, the same spin ensemble also couples to the photon mode of the nominally empty resonator LER-9. The remote spin-photon coupling rate $G_{9,10}/2\pi \simeq 2.5$ MHz is only two times smaller than the local $G_{10}$ and, with $\kappa_9 = 61$ kHz, lies also within the high cooperativity regime $C_{9,10} \equiv G_{9,10}^2/\kappa_9\gamma \sim 14$. Thanks to a combination of circuit mediated capacitive interactions between LER-10 and LER-9 and their high quality factors, hybrid excitations generated at the former are easily detected by measuring the response of the latter.

These data can be understood within the framework of the "two-resonator" circuit QED theory [52], which

generalizes the standard Jaynes-Cummings formalism to the case of multiple cavities. The Hamiltonian describing the hybrid system can be written as follows

$$\mathcal{H} = \sum_{q=i,j} (\omega_{\mathrm{r},q} a_q^\dagger a_q + \Omega_{S,q} S_q^z) + \sum_{q=i,j} G_q (a_q S_q^+ + a_q^\dagger S_q^-) + \kappa_{i,j} (a_i^\dagger a_j + a_j^\dagger a_i) + \mathcal{H}_{\mathrm{dis}}, \quad (1)$$

where $a_q$ and $a_q^\dagger$ represent the photon annihilation and creation operators, respectively, in each $(q = i, j)$ cavity, $S_q^z$, $S_q^+$ and $S_q^-$ represent the conventional spin-1/2 operators, and $\mathcal{H}_{\mathrm{dis}}$ accounts for all terms that cause dissipation, including the couplings of the cavity photons ($\kappa_{\mathrm{c},i}$ and $\kappa_{\mathrm{c},j}$) and the spins ($\gamma_{\mathrm{c},i}$ and $\gamma_{\mathrm{c},j}$) to the readout transmission line. The eigenstates of the first two terms in Eq. (1) define the spin polaritons, the central object of this work. Further details can be found in the theoretical Appendix D 1 below.

For the system of Fig. 3, $i = 9$ and $j = 10$, and only $G_{10}$ and $\Omega_{10}$ are nonzero since LER-9 is empty. Solving for the eigenvalues and eigenstates of (1), as described in Appendix D 1 a, shows that the remote $G_{9,10}$ is a direct manifestation of the interactions brought about by the circuit and gives the relation

$$G_{9,10} = \frac{G_{10}}{\sqrt{2}} \sqrt{1 - \frac{|\omega_{\mathrm{r},9} - \omega_{\mathrm{r},10}|}{\sqrt{|\omega_{\mathrm{r},9} - \omega_{\mathrm{r},10}|^2 + 4\kappa_{9,10}^2}}}. \quad (2)$$

Equation (2) allows estimating $\kappa_{9,10} = 6.5$ MHz, which is reasonably close to the value $\kappa_{9,10} = 5.8$ MHz derived from the circuit simulation (Appendix A 1). The application of input-output theory to this model (see Appendix D 3 a) also provides a good description of the transmission data, as shown by Fig. 3(c) and indicates that LER-9 does not directly couple to the spins but, rather, to the hybrid LER-10 polariton.

### B. Two spin ensembles coupled to a LER pair: Polariton-polariton coupling

Our second study case is illustrated by Fig. 4(a) (see also Fig. 9 in Appendix A 2). Here, LER-1 ($\omega_{\mathrm{r},1}/2\pi = 1.703$ GHz) and LER-2 ($\omega_{\mathrm{r},2}/2\pi = 1.710$ GHz) within a pair host approximately $5 \times 10^{14}$ PTMr and $5 \times 10^{14}$ Tripak$^-$ radical molecules, respectively. This setup aims to couple distant polaritons via the circuit. For comparison purposes, we have also performed the same study on two different PTMr samples, each consisting of $N \sim 5 \times 10^{14}$ spins, placed onto further distant $\simeq$2.1 GHz LER-5 and LER-7 belonging to different pairs [Fig. 4(a)]. This allows comparing experimentally the response of a coupled LER pair to that of two uncoupled LERs. Microwave transmission data measured near the spin resonances $\Omega_{S,i} = \omega_{\mathrm{r},i}$ are shown in Figs. 4(b) and 4(c), while results obtained

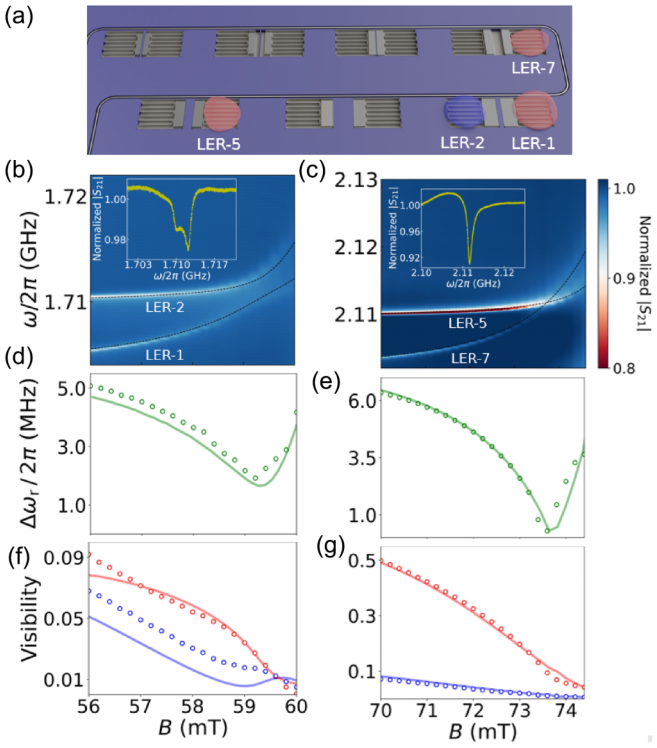


FIG. 4. (a) Experimental setup for polariton-polariton coupling. LER-1 and LER-2, forming a coupled pair, host PTMr (orange) and Tripak$^-$ (blue) molecular spin ensembles, respectively, whereas LER-5 and LER-7, belonging to distant, thus uncoupled pairs, each host a different PTMr molecular ensemble. All these molecular samples consist of $N \sim 5 \times 10^{14}$ molecules. Panels (b),(d),(f) and (c),(e),(g) provide experimental data and simulations obtained for the coupled and the uncoupled LERs, respectively: color plots of the microwave transmission measured at $T = 11$ mK for a $-50$ dBm input power, equivalent to photon numbers $n \sim 5.5 \times 10^9$ for LER-1, $n \sim 5.06 \times 10^{10}$ for LER-2, $n \sim 4.62 \times 10^9$ for LER-7, $n \sim 3.27 \times 10^{10}$ for LER-5, near the resonances of each spin ensemble with its local LER (b),(c); experimental (dots) and theoretical (lines) frequency differences between the two upper polaritons as a function of magnetic field (d),(e); experimental (dots) and theoretical (lines) visibilities of these modes as a function of magnetic field (f),(g). The insets in panels (b),(c) are frequency-dependent transmission data measured at the (anti-)crossing magnetic fields $B = 59.2$ mT and $B = 73.6$ mT, respectively. The fits are based on the model outlined in the text [Eq. (1)] and detailed in Appendix D 1 b, with parameters $G_1/2\pi = 19.5$ MHz, $G_2/2\pi = 8.5$ MHz and $\kappa_{1,2}/2\pi = 1.06$ MHz for the coupled LER pair and $G_7/2\pi = 22$ MHz, $G_5/2\pi = 9.7$ MHz and $\kappa_{5,7}/2\pi = 0$ for the uncoupled LERs.

over wider frequency and magnetic field regions are given in Appendixes B and D 3 b.

The local spin-photon couplings reach high cooperativity for LER-2 and LER-5 ($G_2/2\pi = 8.5$ MHz, $G_5/2\pi = 9.7$ MHz) and the strong coupling regime for LER-1 and LER-7 ($G_1/2\pi = 19.5$ MHz, $G_7/2\pi = 22$ MHz). The wide range of coupling strengths is likely associated

with the very inhomogeneous distribution of the molecules over the surface of the LER inductors (see Appendix A 2). This difference and, to a lesser extent, the different spin resonance frequencies of PTMr and Tripak$^-$ (see Figs. 2 and 10 in Appendix A 2) allow tuning the upper polariton branches of different LERs relative to each other, eventually bringing them into mutual resonance as shown in Figs. 4(b) and 4(c). In the case of the uncoupled LER-5 and LER-7 [Figs. 4(c) and 4(e)], the two branches then simply cross. By contrast, for the coupled LER pair [Figs. 4(b) and 4(d)] there is an avoided level crossing with a gap $\Delta\omega_{\rm p}^{+}/2\pi \simeq 1.9$ MHz near 59.2 mT. This behavior resembles the mode splitting of two identical coupled LERs, shown in Fig. 1(c), only here we deal with polaritons and the tuning is achieved *in situ* by the magnetic field, exploiting their different spin components. By analogy, we conclude that the gap $\Delta\omega_{\rm p}^{+}$ is a direct manifestation of the polariton-polariton interaction that allows estimating the coupling constant $J_{1,2}^{+}/2\pi \simeq \Delta\omega_{\rm p}^{+}/4\pi = 0.96$ MHz. Furthermore, near the anticrossing the visibilities of the two coupled polariton branches, shown in Fig. 4(f), go through a local minimum and a local maximum, i.e., these modes become then "brighter" and "darker." This effect is not observed for the two uncoupled LERs [$\kappa_{i,j} = 0$, Fig. 4(g)]. In conclusion, these experiments show that the circuit can induce interactions between remote polaritons that are coherent, in the sense that they overcome the polariton linewidths [inset in Fig. 4(b)]. In addition, they suggest that the coupled states become symmetric and antisymmetric combinations of the local excitations, which couple constructively and destructively to the common readout line.

Theoretical calculations based on Hamiltonian (1) help again in getting a deeper insight into these results. In this case, and as sketched in Fig. 5(a), both LERs interact with a different spin sample, with respective coupling strengths $G_i$ and $G_j$. As shown in Figs. 4(d) and 4(e), this model accounts for the onset of a finite gap between the two polariton branches when $\kappa_{i,j} \neq 0$, which is adequately described by the following expression, derived in Appendix D 1 b:

$$\Delta\omega_{\rm p}^{+} = 2J_{i,j}^{+} = 2\kappa_{i,j}\cos\frac{\theta_i}{2}\cos\frac{\theta_j}{2}, \tag{3}$$

where $\theta_i = \tan^{-1}(2G_i/\Delta_i)$, with $\Delta_i = \Omega_{S,i} - \omega_{{\rm r},i}$ (and equivalently for LER-$j$) measure the spin components of the two polaritons. The same model, combined with the input-output formalism that includes the couplings of photon and spin components to the readout line, describes well the overall features observed in the microwave transmission experiments [see Fig. 5(a) and Appendixes D 1 b, D2 and D 3 b for details]. This is confirmed by comparing the simulations in Figs. 5(b) and 5(c) to the experimental results shown in Figs. 4(c) and 4(b), respectively.

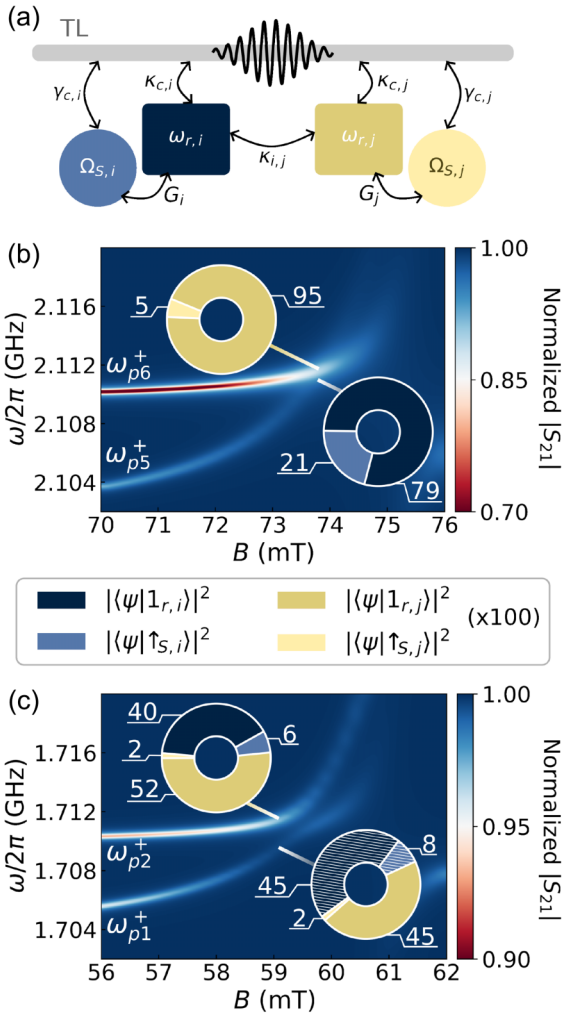


FIG. 5. (a) Sketch of the polariton-polariton coupling model showing the main interactions present in the system [Eq. (1)]. Details of the eigenstates and of the microwave transmission calculations are described in Appendix D. (b) Simulated 2$D$ microwave transmission plot for two uncoupled ($\kappa_{i,j} = 0$) LERs. (c) Simulated 2$D$ microwave transmission plot for two LERs coupled by $\kappa_{i,j} = 1.06$ MHz. The insets show the probabilities of the single spin and single photon excitation states in each polariton. Striped sectors in the inset of panel (c) signal negative probability amplitudes.

In particular, it accounts well for the changes in polariton visibilities that take place near the polariton-polariton anticrossing [Figs. 4(f) and 4(g)]. As discussed in Appendix D 3 b, the fact that the "dark" polariton state retains then some visibility can be linked to the direct coupling of spins to the readout line (i.e., that $\gamma_{\rm c,1}$ and $\gamma_{\rm c,2} \neq 0$), and to its asymmetry (i.e., that $\gamma_{\rm c,1} \neq \gamma_{\rm c,2}$). In these simulations, we left $\kappa_{i,j}$ as the only free parameter and obtained the rest from either circuit simulations or from independent fits to the data. The estimated $\kappa_{1,2}/2\pi = 1.06$ MHz turns out to be a factor of two smaller than $\kappa_{1,2}/2\pi = 2.4$ MHz obtained from the circuit

simulations (Appendix A 1). We associate the disagreement with uncertainties in the "bare" resonance frequencies of the two uncoupled LERs, which are affected by the dielectric constant of the molecular deposits located onto their respective capacitors (see Appendix A 2 and Fig. 9). Since this detuning is not independently known after the molecular deposition, $\kappa_{1,2}$ is best regarded as an effective fitting parameter that partly absorbs this uncertainty, rather than as an independent determination of the geometric capacitive coupling (see Appendix D 1 b).

In what follows, we further exploit the theory to move beyond spectroscopic features and gain some physical intuition on the nature of the polaritonic states and on how they are modified by their mutual interaction and by external parameters. The wave functions of the polaritons calculated in the basis of local single-photon and single-spin excitations are shown as insets to Figs. 5(b) and 5(c). For $\kappa_{i,j} = 0$, spin and photon excitations hybridize locally, but there are no correlations between "left" and "right" excitations. By contrast, for $\kappa_{i,j} \neq 0$ the polaritons acquire finite amplitudes of spin and photon excitations arising from both LERs (Fig. 23 in Appendix D 1 b) when they are brought into resonance by the magnetic field. Near the anticrossing, the photonic component approaches symmetric and antisymmetric combinations of the local photon modes. The model also predicts that the entanglement between the photon modes from both LERs becomes then maximum (Fig. 24 in Appendix D 1 b). The opposite limit of far detuned, nearly localized polaritons leads to a circuit mediated effective transverse interaction $J(S_i^+ S_j^- + S_i^- S_j^+)$ between the excitations of the two spin ensembles, very much as in the case of two spin ensembles coupled to the same cavity mode in the dispersive regime [10,19,33].

### C. Polariton-polariton dispersive readout

The dual, light-matter character of the polariton excitations and their mutual, circuit-mediated interaction can be probed by performing pump-probe experiments with microwave pulses that use one of the polaritons to sense the excitation of the other one. The protocol and the experimental setup are sketched in Fig. 6 and in Appendix A 5, respectively. A high power short "pump" pulse resonantly excites a polariton on one side of the LER pair. This is then followed by a set of "probe" pulses with frequencies scanning that of the other polariton that allows detecting any changes in its resonance frequency.

Results of reference experiments performed at zero field, when the LER excitations are pure photonic modes, are also shown in Figs. 6 and Appendix C 1. They show no measurable shift, as expected for two coupled resonators whose frequencies must remain insensitive to changes in their respective populations. By contrast, when $B = 57$ mT, near the avoided level crossing in Fig. 4(b), both polaritons acquire a finite spin component [see Fig. 5(c)]. In this case, the initial excitation of one mode,

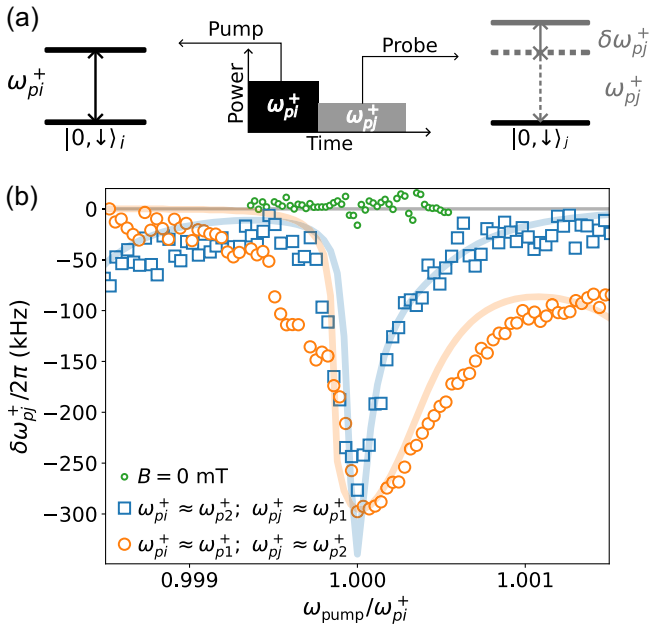


FIG. 6. Polariton-polariton pump-probe measurements. (a) Sketch of the measurement protocol. A short high power microwave pulse resonantly excites one polariton at a frequency $\omega_{\mathrm{p},i}^+$. Then, a series of lower power pulses probe the frequency shift $\delta\omega_{\mathrm{p},j}^+$ generated on the other polariton. (b) Experimental frequency shift measured at $T = 11$ mK by pumping LER-1 polariton ($\omega_{\mathrm{p},1}^+/2\pi \simeq 1.706$ GHz) and detecting changes in the LER-2 polariton (orange circles) and vice versa (blue open squares). Data measured at $B = 0$ are also shown as green circles. Excitations at both LERs correspond then to pure photon modes and no dispersive shift is observed. In these experiments LER-1 was coupled to a PTMr spin ensemble whereas LER-2 was coupled to a Tripak$^-$ sample. The lines are theoretical predictions for the dynamical response of the system sketched in Fig. 5(a) obtained by solving the time-dependent master equations as described in [53].

at a frequency $\omega_{\mathrm{p},i}^+$ does generate a measurable shift $\delta\omega_{\mathrm{p},j}^+$ in the frequency $\omega_{\mathrm{p},j}^+$ of the other one. Examples of the readout process and results obtained at different magnetic fields are given in Appendix C 2. This nonlocal dispersive response provides a direct experimental signature of the coupling between two remote polaritons, and of the fact that it is tuned through their spin component. Inserting this circuit mediated interaction in the model described in Appendix D then allows estimating how remote correlations are introduced in the elementary system excitations.

The measurement of the frequency shift can be exploited to perform polariton spectroscopy. For this, $\omega_{\mathrm{pump}}$ is swept across $\omega_{\mathrm{p},i}^+$. The ensuing $\delta\omega_{\mathrm{p},j}^+$ then maps the distribution of polariton excitation frequencies. The results, shown in Fig. 6(b), agree with the polariton line shapes derived from transmission experiments (Fig. 4). These measurements also show that the two polaritons can play both roles, either as the quantum system that is

"pumped" or as its "probe." They are also in good agreement with theoretical predictions [solid lines in Fig. 6(b)] that have been obtained by solving the master equations governing the time-dependent response of the coupled system, as described in [53]. These results give further insight into the upper polariton wave functions. We find polariton linewidths $\kappa_1^+/2\pi \simeq 0.5$ MHz and $\kappa_2^+/2\pi \simeq 0.2$ MHz, which lie in between the pure photon and spin linewidths, as expected. Their values are determined by the ratio $G_i/\Delta_i$: the stronger the local spin-photon coupling is (in this case at LER-1) the broader polariton excitations become.

## IV. CONCLUSIONS AND OUTLOOK

In summary, we have tested, under diverse conditions, a platform whose basic nodes are hybrid spin-photon polaritons formed at different superconducting LERs. The results show that each of these nodes can be addressed and read out by quite standard microwave transmission experiments. Besides, they can be deterministically coupled via the circuit, with coupling strengths $\sim\Delta\omega_p^+/2$ that can be made strong enough to overcome polariton losses. In spite of the fact that the LERs mutual capacitive couplings are fixed by the circuit geometry, their effect on the spin and photon polariton components can be tuned by changing magnetic field, and also driving power (Appendix B 2) or temperature (Appendix B 3).

The modular character and flexibility of this platform can provide key resources for the future development of hybrid quantum technologies based on magnetic molecules [37,38,43–45]. By establishing spin-photon polaritons as addressable nodes in superconducting quantum circuits, it sets a promising basis for scaling up quantum simulation and quantum computing with these systems beyond the Hilbert space of each molecular entity, which has so far limited proof-of-concept experiments [34,42,54–57]. This approach benefits from the nearly unbound possibilities for designing molecules with a given magnetic response, which determines the magnetic field dependence of the polariton frequencies as well as their interaction with microwave cavity photons [58]. On the side of the circuit, LERs can be designed to enhance the single spin-photon coupling to values that might allow working with individual molecular spins [53,59]. Also, the chip layout can be easily expanded to include additional lines to control the spin frequency at each module. This property might also be of interest for developing elements of superconducting electronics. Model simulations shown in Appendix D 1 suggest that effective interactions and entanglement between distant microwave photons can be generated and tuned *in situ* by using external parameters, in particular the magnetic field, as "control knobs." This scheme then offers an alternative route to realize switches [52] or filters [60], which are based on tunable couplings between two or more resonators.

## ACKNOWLEDGMENTS

The authors acknowledge useful discussions with M. J. Martínez-Pérez. This work has received support from Grants No. TED2021-131447B-C21, No. TED2021-131447B-C22, No. PID2022-140923NB-C21, No. PID2022-141393OB-I00, No. CEX2023-001263-S and No. CEX2023-001286-S funded by MCIN/AEI/10.13039/501100011033, ERDF "A way of making Europe" and ESF "Investing in your future", from the Gobierno de Aragón Grant No. E09-23R-QMAD, from the European Union Horizon 2020 research and innovation programme through FET-OPEN Grant No. FATMOLS-No862893, from the Novo Nordisk Foundation Exploratory Interdisciplinary Synergy Programme 2021 through Grant No. NNF21OC0070832, from QUANTERA project OpTriBits (AEI: PC2024-153480), and from the Spanish Ministry for Digital Transformation and Civil Service and Next Generation EU through the Quantum Spain project (Digital Spain 2026 Agenda). It also forms part of the Advanced Materials and Quantum Communication programmes with funding from European Union Next Generation EU (PRTR-C17.I1), MCIN, Gobierno de Aragón, and CSIC (QTEP-PT-001). D. P. acknowledges the financial support of the National Science Centre Poland within the Opus Project No. 2020/37/B/ST5/02735.

## DATA AVAILABILITY

The data that support the findings of this article are openly available at the FATMOLS community of the Zenodo repository [61].

## APPENDIX A: EXPERIMENTAL DETAILS

### 1. Circuit design and fabrication

The superconducting chip used in the experiments, shown in Fig. 1(a), contains a single impedance-matched transmission line and 14 side-coupled LERs. LERs [20,23,25,29,30,46,53,62] are circuits made of an inductor $L$ and a capacitor $C$ connected in series, as shown in Fig. 7(a). The capacitor consists of several interdigitated fingers. Its capacitance is defined by the finger length, width, and separation. Regarding the inductor, a meander-like design is used. The inductance is mainly determined by the length and width of the superconducting metal stripe.

The "bare" resonance frequency of each isolated LER$-i$ is $\omega_{r,i} = 1/\sqrt{LC_i}$, with $i = 1, \ldots, 14$. Every LER in the chip has a slightly different $\omega_{r,i}$ (Table I). For this purpose, all LERs have the same $L \simeq 6$ nH whereas $C_i$ is varied by changing the number of fingers and their length. The 7-turn inductor is made of a 4 μm wide strip with the dimensions indicated in Fig. 7(a). The capacitors contain from 10 to 26, 6 μm wide fingers

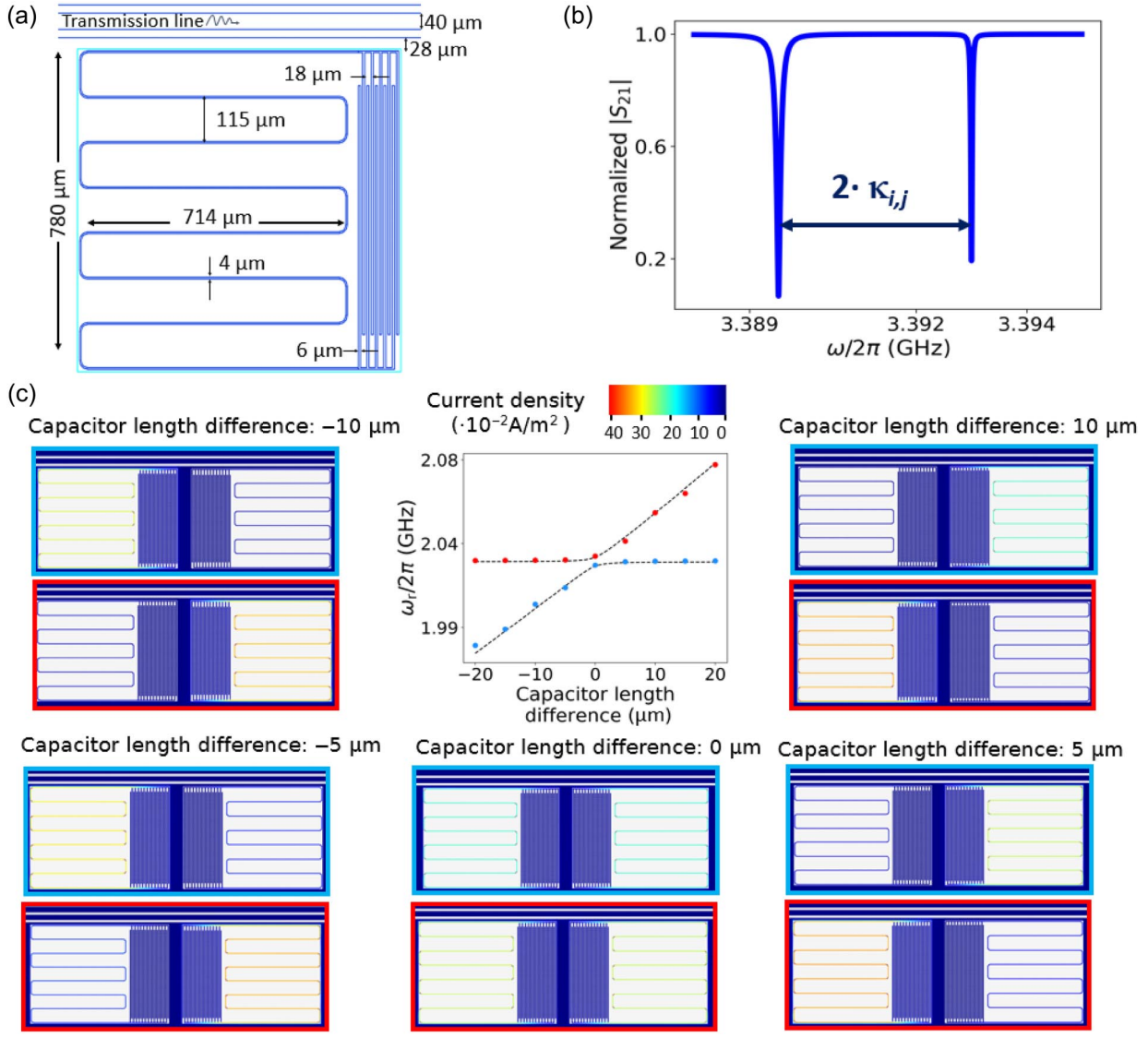


FIG. 7. (a) Sketch of a superconducting LER showing the *LC* circuit dimensions. (b) Electromagnetic simulation, using the Sonnet software, of two capacitively coupled LERs. The microwave transmission through the readout line, normalized to the maximum transmission, shows two sharp dips that correspond to absorption by symmetric and antisymmetric resonant modes with frequencies separated by twice the coupling constant $\kappa_{i,j}$. (c) Single-photon current density maps simulated with Sonnet for different values of the detuning between the bare LER frequencies. The modes become more localized as the detuning is increased.

separated by 6 μm gaps. Their length varies from 690 to 750 μm. The geometrical capacitance (without taking into account any parasitic capacitance) ranges between 0.99 and 0.28 pF. The coupling to the feed-line $\kappa_{c,i}$ depends on the distance of the resonator to the transmission line. This chip was designed for coupling values $\kappa_{c,i} \approx 17$–$42$ kHz.

LERs in the chip are distributed in pairs. LERs $(i, j)$ forming a pair are oriented with their capacitors facing each other, as illustrated by Fig. 7. This geometry induces a capacitive coupling whose strength $\kappa_{i,j}$ is different for each pair and depends on the distance between them.

The LER and readout line geometries were designed using AutoCAD. The microwave transmission through the line near the LER resonances was simulated using Sonnet [63]. When both LERs of a pair are identical the frequency splitting between the two resonant modes $\Delta\omega_r = 2\kappa_{i,j}$ [Fig. 7(b)], which allows estimating the capacitive coupling strength. We design the circuit such that $\kappa_{i,j}/2\pi$ ranges from 0.3 to 30 MHz (Table I). In order to allow individually addressing the LERs within each pair, they are detuned by approximately 20–30 MHz, such that the condition $\Delta\omega_r > \kappa_{i,j}$ is approximately fulfilled. Moreover, nearest LER pairs are separated by 0.7–1.0 mm and detuned 250 MHz from each other to prevent unwanted crosstalk.

The chip fabrication process starts with the pretreatment of a 275 μm thick Si substrate in a 1% hydrofluoric acid bath to remove the native silicon oxide layer. A 125 nm

TABLE I. Characteristic parameters of the 14 bare LER resonances and their mutual capacitive couplings obtained from electromagnetic simulations with Sonnet.

| LER | $\omega_r/2\pi$ (GHz) | $\kappa/2\pi$ (kHz) | $\kappa_c/2\pi$ (kHz) | $\kappa_{i,j}/2\pi$ (MHz) |
|---|---|---|---|---|
| 1 | 2.008 | 20 | 17 | 2.4 |
| 2 | 2.038 | 22 | 19 | |
| 3 | 2.247 | 29 | 26 | 0.33 |
| 4 | 2.278 | 31 | 29 | |
| 5 | 2.512 | 38 | 35 | 0.965 |
| 6 | 2.544 | 40 | 37 | |
| 7 | 2.586 | 35 | 32 | 33 |
| 8 | 2.622 | 39 | 36 | |
| 9 | 2.740 | 32 | 29 | 5.75 |
| 10 | 2.755 | 32 | 29 | |
| 11 | 3.119 | 42 | 39 | 9 |
| 12 | 3.150 | 43 | 41 | |
| 13 | 3.392 | 42 | 39 | 2.66 |
| 14 | 3.425 | 45 | 42 | |

thick superconducting NbTiN film is then deposited onto the Si substrate by using confocal dc AJA magnetron sputtering, with a chamber base pressure below $2 \times 10^{-8}$ Torr. The deposition conditions were controlled with an argon flow of 15 sccm and a nitrogen flow of 1 sccm as plasma processing gases, maintaining a chamber pressure of 2 mTorr and a power setting of 200 W. These conditions lead to a deposition rate of 1.21 Å/s. Afterward, maskless laser writer lithography with a MicroWriter ML3 Pro system is employed to pattern the chip design onto the NbTiN film. For this, a layer of negative photoresist (AZ2070) is spin-coated onto the surface and exposed to a 405 nm laser at room temperature. Following the development of the resist, reactive ion etching is performed. The etching gases, $SF_6$ and Ar, were flowed at rates of 20 and 10 sccm, respectively. The process operated at 75 W of rf power and a chamber pressure of 10 mTorr. The process concludes with the removal of the remaining photoresist by boiling in acetone, followed by rinsing with isopropanol.

### 2. Molecular integration and characterization

The PTMr and Tripak$^-$ organic free radical molecules were dissolved in chlorobenzene, with concentrations ranging from 0.08 to 8 mM, together with polystyrene. Then, 0.1 µl drops were transferred onto different parts of the circuit, namely the LER inductors or the transmission line, and left dry under red light, as shown in Fig. 8. The resulting solid deposits are very stable at ambient conditions. They contain a nominal spin number $N$ determined by the drop volume and concentration, namely $N \simeq 5 \times 10^{12}$, $N \simeq 5 \times 10^{13}$ and $N \simeq 5 \times 10^{14}$ for, respectively, 0.08, 0.8 and 8 mM solutions. Although

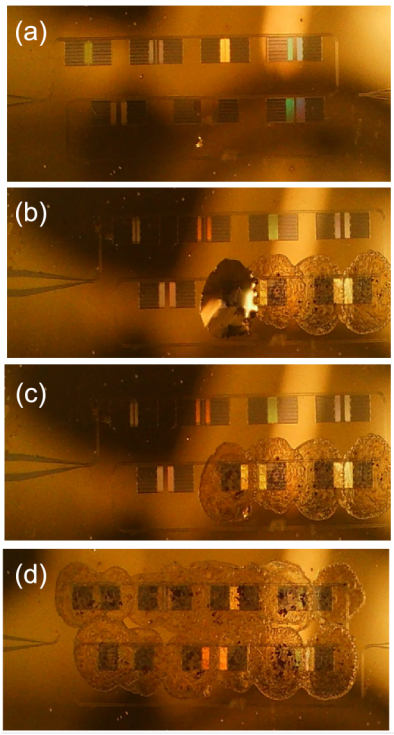


FIG. 8. Optical microscopy images showing different steps in the deposition of Tripak$^-$ from a 0.8 mM solution in chlorobenzene. Starting from the bare chip [panel (a)], in each step, a new drop is deposited on top of a LER inductor [panel (b)] using a micropipette and then left dry under red light [panel (c)] until all LER inductors are covered with the desired sample [panel (d)]. The dry deposits consist of the free radical molecules dispersed in polystyrene.

polystyrene prevents aggregation of the free radical molecules, the coverage of the LER inductor by the dry deposits turns out to be quite inhomogeneous (Fig. 9), thus leading to different spin-photon couplings even for drops with nominally the same number of spins. The molecular deposits cover also (part of) the capacitor. Their dielectric constant then modifies the capacitance and also the LER frequencies, and the detuning within

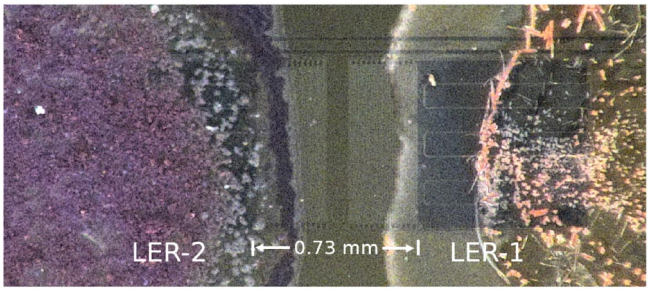


FIG. 9. Close-up microscopy image of the coupled LER-1 and LER-2, hosting $N \sim 5 \times 10^{14}$ PTMr and Tripak$^-$ free radical molecules, respectively.

each pair, from their bare values. In order to cover different LERs within a pair with a different free radical sample, the drops were landed onto the region separating two neighbor inductors from different LER pairs. An example is shown in Fig. 8(b).

The spin resonance frequencies $\Omega_S$ of both samples were characterized by broadband magnetic spectroscopy, performed by measuring the microwave transmission through a superconducting waveguide coupled to a molecular deposit [50,51]. Results are shown in Figs. 2(c), 2(d), 10(a), and 10(b). Figures 10(c) and 10(d) show that $\Omega_S \simeq g\mu_B SB/\hbar$. From the linear slope we find $g = 2.001$ for PTMr and $g = 2.003$ for Tripak$^-$. The slightly different magnetic responses of PTMr and Tripak$^-$ [Fig. 10(e)] contribute to make the polaritons formed by their interaction with different LERs tunable relative to each other (e.g., as in the case of LER-1 and LER-2, shown in Fig. 4).

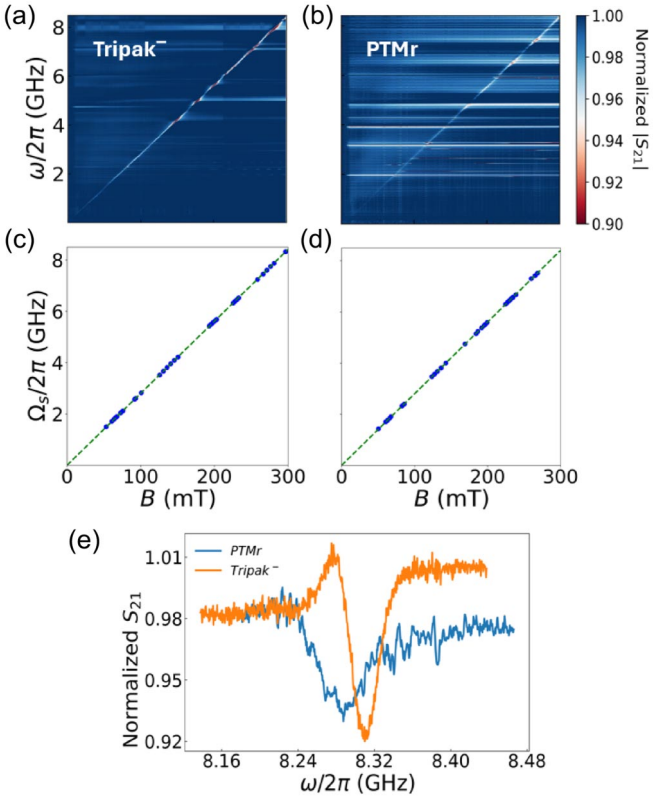


FIG. 10. Spin characterization by broadband magnetic spectroscopy. Two-dimensional plots of the microwave transmission of a superconducting waveguide coupled to Tripak$^-$ (a) and PTMr (b), measured at $T = 11$ mK as a function of frequency and magnetic field. Magnetic field dependence of the spin resonance frequency for Tripak$^-$ (c) and PTMr (d). The lines are least-squared fits based on $\Omega_S = g\mu_B B/\hbar$ giving $g = 2.003$ for Tripak$^-$ and $g = 2.001$ for PTMr. (e) Scans of the normalized transmission measured at $B = 296.13$ mT, showing the frequency shift in the absorption of PTMr and Tripak$^-$ spins associated with their slightly different $g$ factors.

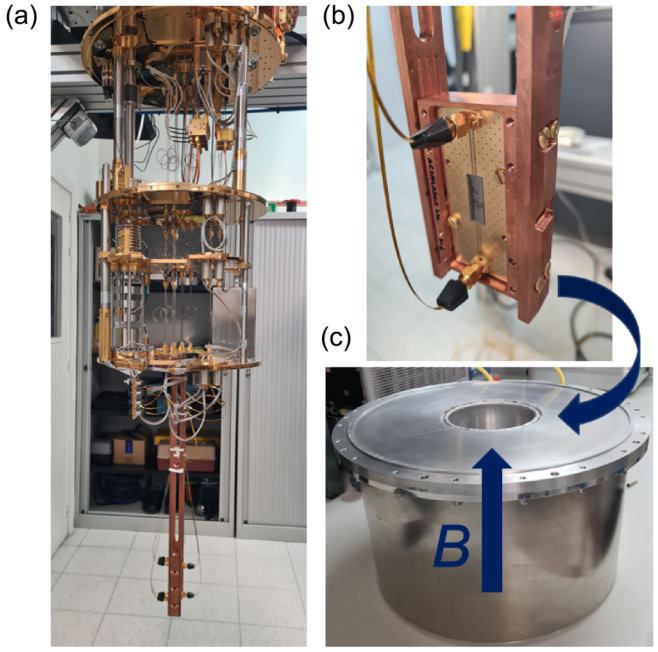


FIG. 11. Microwave transmission setup. (a) Image of the cryo-free $^3$He-$^4$He dilution refrigerator used for both the cw microwave transmission experiments and the pump-probe experiments with microwave pulses. (b) Cold finger hosting the superconducting chip at the center of the 1 T cryo-free superconducting magnet (c). The magnetic field $\vec{B}$ is applied in the chip's plane, parallel to the readout transmission line.

### 3. Cryogenic setup

Experiments reported in this paper are performed at temperatures $T \geq 11$ mK by thermally anchoring the chips to the mixing chamber of a $^3$He-$^4$He cryo-free dilution refrigerator [Fig. 11(a)]. A copper cold finger [Fig. 11(b)] places the chip at the center of a 1 T axial superconducting magnet [Fig. 11(c)]. The magnetic field $\vec{B}$ is applied along the $\hat{z}$ axis of the laboratory reference frame, which is parallel to the chip's readout waveguide. Cryogenic coaxial lines transmit the input and output microwave signals. The input signal was attenuated by two or more $-10$ dB attenuators before reaching the chip, depending on the specifics of each experiment. Continuous wave (cw) microwave transmission experiments were performed with either $-50$ dB (LER-9 and LER-10, Fig. 3) or $-40$ dB (LER-1, LER-2, LER-5 and LER-7, Fig. 4) attenuation, while pump probe polariton-polariton dispersive readout measurements (Fig. 6) used $-20$ dB. The output signal was amplified $+30$ dB at $\sim$4 K with a low-noise cryogenic amplifier.

### 4. Microwave transmission experiments

The cw microwave transmission through the device was measured using a Vector Network Analyzer (VNA). The VNA generates a microwave signal, with a frequency $\omega/2\pi$ ranging from 0.01 up to 14 GHz, which is fed into

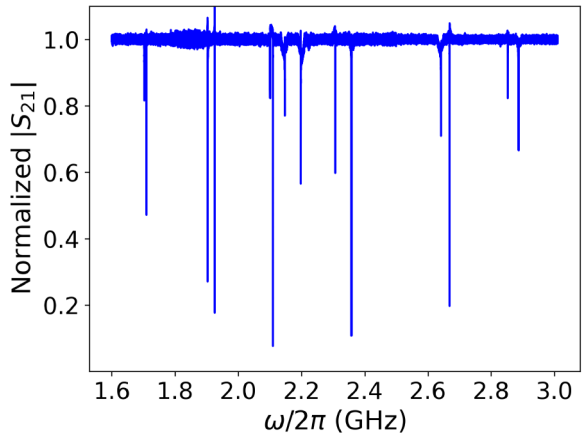


FIG. 12. Microwave transmission through the readout line of the device shown in Fig. 1(a), measured at $B = 0$ and $T = 11$ mK. Fourteen sharp dips are apparent, corresponding to the resonant modes of all LERs in the chip.

the chip's readout line. The output signal is then amplified at 4 K and detected by the VNA to determine the $S_{21}$ transmission parameter.

Illustrative microwave transmission results, measured at $T = 11$ mK and normalized to the maximum transmission, are shown in Fig. 12. The LER resonances give rise to very narrow dips in transmission. Each of them can be described by the following expression:

$$S_{21} = 1 - \frac{\kappa_c}{i(\omega_r - \omega) + \kappa}, \tag{A1}$$

where $\kappa$ is the LER photon decay rate and $\kappa_c$ is the coupling rate to the readout line.

The stationary number of photons $n$ in LER-$i$ for any given input power $P$ follows from the steady-state solution of the input-output equations of motion for a single driven LER [64]. Writing the input photon flux as $|\alpha_{in}|^2 = P/\hbar\omega$, the field in the cavity is $\langle a_i \rangle = -i\sqrt{\kappa_{c,i}}\,\alpha_{in}/[i(\omega_{r,i} - \omega) + \kappa_i]$, which on resonance reduces to $\langle a_i \rangle = -i\sqrt{\kappa_{c,i}}\,\alpha_{in}/\kappa_i$. The stationary photon number $n = |\langle a_i \rangle|^2$ is therefore given by

$$n = \frac{P\kappa_{c,i}}{\kappa_i^2 \hbar\omega_{r,i}}. \tag{A2}$$

### 5. Experiments with microwave pulses

Figure 13 illustrates the microwave pulse generation and detection stages used in the pump-probe experiments. It consists of a digital arbitrary waveform generator (AWG) that sends short and high power pump pulses to resonantly excite either the spins or the polariton modes. These are followed by a train of lower power readout pulses to detect any changes produced in the LER or polariton modes. A microwave switch, triggered by the AWG, feeds excitation and readout pulses into separate lines at the initial room temperature stage. The probe signal then splits into a local oscillator reference for the readout stage (LO) and the signal that is fed into the cryogenic stage. Pump and probe signals are combined again into a single physical line and fed through the same port of the cryostat. At the output of the cryogenic stage, a second switch deviates the pump pulse to a fast microwave oscilloscope in order to avoid damaging the detection electronics. The readout pulse is guided to an $IQ$ mixer, fed with the LO and rf signals, that extracts the two rf quadrature components. These components are then digitized by the oscilloscope and sent to the computer for post-processing.

## APPENDIX B: CW MICROWAVE TRANSMISSION

### 1. Coupled vs uncoupled LERs

Figures 14(a) and 14(b) show the results of cw microwave transmission measurements for LER-1 and LER-2,

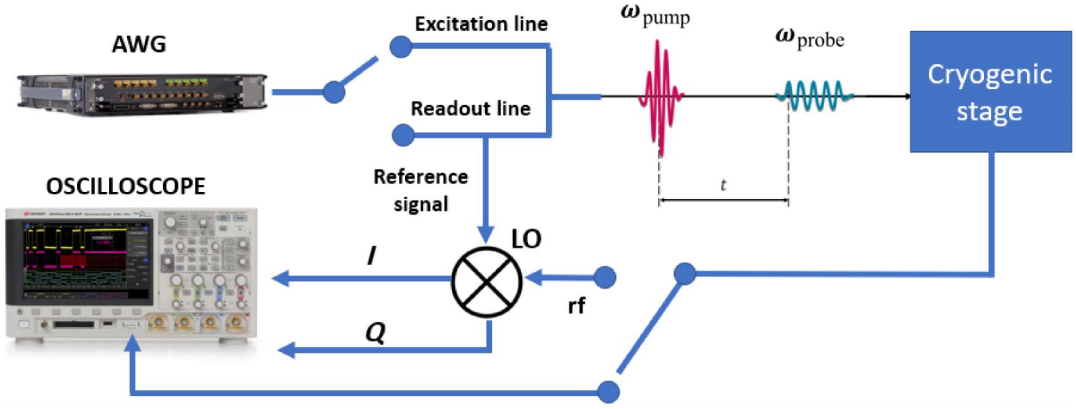


FIG. 13. Microwave pulse generation and detection stages. A fully digital microwave AWG generates the excitation and readout signals. The readout signal coming out of the cryogenic stage is first down-converted by a synchronous $IQ$ mixer and then its two quadrature components are digitized by a fast digital oscilloscope.

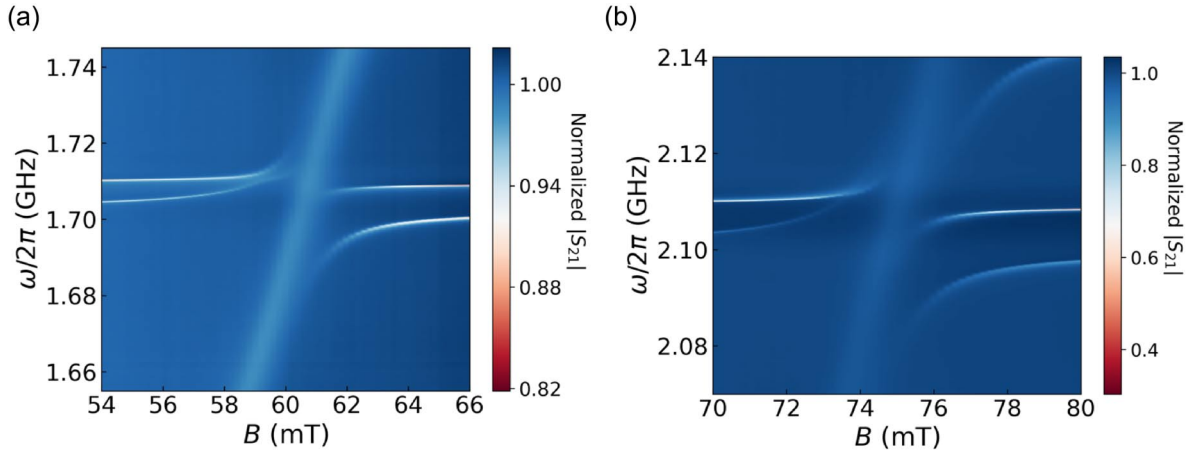


FIG. 14. $2D$ plot of the microwave transmission measured at $T = 11$ mK for a $-50$ dBm input power, equivalent to photon numbers $n \sim 5.5 \times 10^9$ for LER-1, $n \sim 5.06 \times 10^{10}$ for LER-2, $n \sim 4.62 \times 10^9$ for LER-7, $n \sim 3.27 \times 10^{10}$ for LER-5, near the resonance frequencies of: (a) LER-1 (coupled to PTMr) and LER-2 (coupled to Tripak$^-$) belonging to a coupled pair; (b) LER-5 (coupled to PTMr) and LER-7 (coupled to PTMr), belonging to different pairs, thus being mutually uncoupled. The signal arising from the direct coupling of spins to the readout transmission line is visible and gives *in situ* information on the spin resonance frequency.

and for LER-5 and LER-7 in wider magnetic field and frequency regions as compared to those shown in Fig. 4. As it is discussed in Sec. III B, the former two LERs form a coupled pair, whereas the latter belong to two different pairs, thus they are mutually uncoupled. All these LERs host free-radical deposits with $N \sim 5 \times 10^{14}$ spins. The results confirm the anticrossing occurring between the upper polariton branches of the two coupled LER-1 and LER-2. The finite gap $\Delta\omega_p^+$ reflects the polariton-polariton coupling generated by the circuit. By contrast, when the polariton branches of uncoupled LER-5 and LER-7 are brought into resonance by the magnetic field $\Delta\omega_p^+ = 0$. These data also show that the two lower polaritons, which become visible in transmission at higher magnetic fields ($B \gtrsim 75$ mT), do not merge for any of these LER pairs, thus the transmission data show no interaction effects for these polariton branches.

### 2. Power dependence of the microwave transmission and the spin-photon coupling

cw microwave transmission measurements were performed for different input powers. Illustrative results, obtained for the 3.274 GHz LER-13 coupled to $N \sim 5 \times 10^{13}$ Tripak$^-$ molecules, are shown in Fig. 15(a).

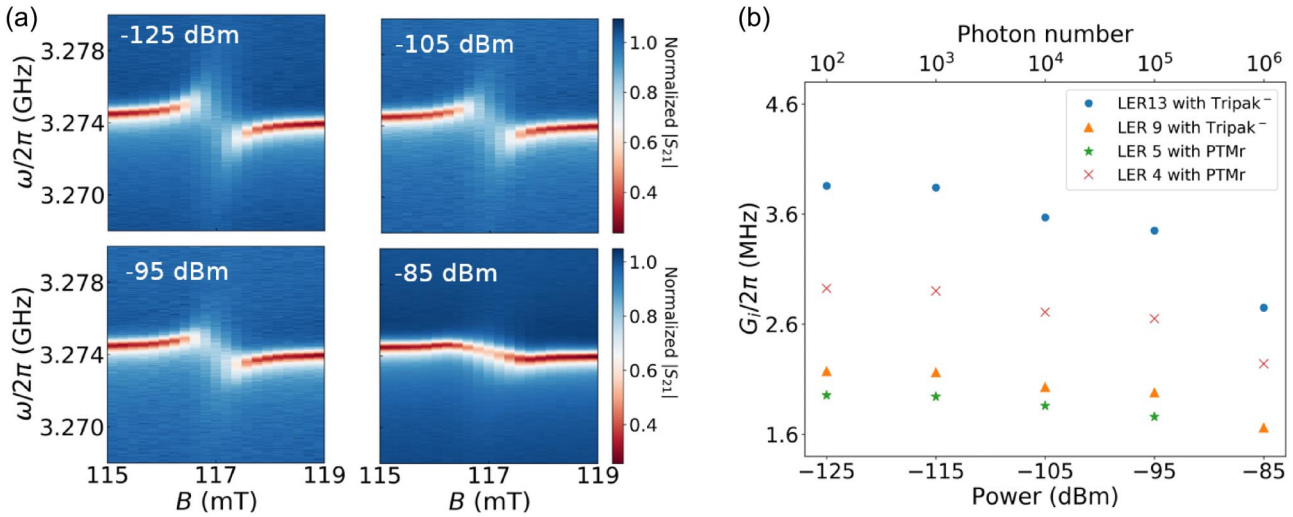


FIG. 15. (a) $2D$ microwave transmission plots measured, at $T = 11$ mK and for different input powers, near the resonance of LER-13 with $N \sim 5 \times 10^{13}$ Tripak$^-$ spins. The avoided level crossing induced by the collective spin-photon coupling gradually decreases as the input power is increased. (b) Power dependence of the spin-photon coupling strength $G_i$ obtained by fitting microwave transmission data using input-output theory (Appendix D 2). Data are given for LER-13 and LER-9, hosting $N \sim 5 \times 10^{13}$ Tripak$^-$ molecules, and for LER-5 and LER-4, hosting $N \sim 5 \times 10^{13}$ PTMr molecules.

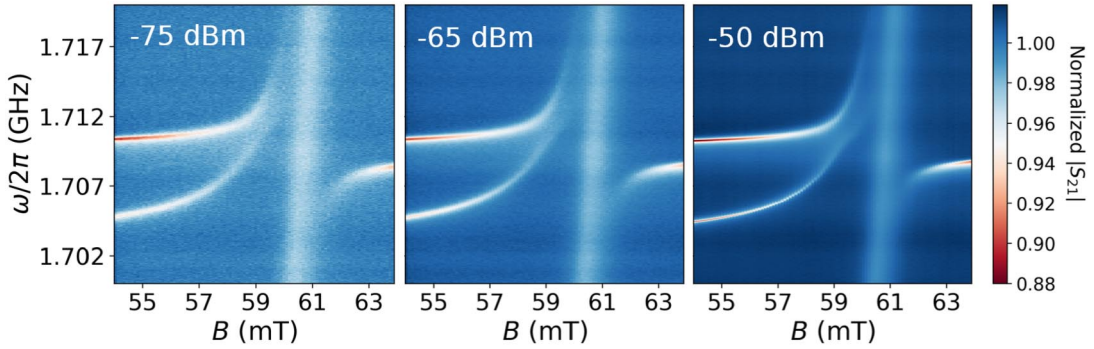


FIG. 16. $2D$ microwave transmission plots measured, at $T = 11$ mK and for three different input powers, near the resonances of LER-1 and LER-2 with $N \sim 5 \times 10^{14}$ PTMr and Tripak$^-$ organic free-radicals, respectively. The data show also the signal arising from the direct coupling of the molecular spins to the readout transmission line. This signal bears evidence of their paramagnetic behavior.

Typical signatures characterizing the resonant collective coupling to the molecular spins are observed for all input powers. Yet, they become less visible with increasing power, suggesting that the effective spin-photon strength $G_{13}$ decreases. This is confirmed by the data of Fig. 15(b), which show $G_{13}$ as a function of power. Data measured for three other LERs coupled to either Tripak$^-$ or PTMr deposits of similar size, show the same qualitative behavior. The drop in local spin-photon coupling does not seem to be associated with any cavity saturation, because the estimated number of photons $n \leq 10^6$ is between 7 and 11 orders of magnitude lower than the number of spins $N$.

Figure 16 shows results obtained for LER-1 and LER-2 at even higher input powers, which, in spite of the ten times larger spin concentration ($N \sim 5 \times 10^{14}$), lead to higher $n/N$ ratios $\sim 10^{-7} - 10^{-4}$. In this case, no major changes in neither the local spin-photon couplings $G_1$ and $G_2$, nor in the polariton-polariton anticrossing $\Delta\omega_p^+$ are observed. A tentative interpretation is that the cavity induces some spin saturation due to the slow spin relaxation (see below), which likely depends on spin concentration. This effect is

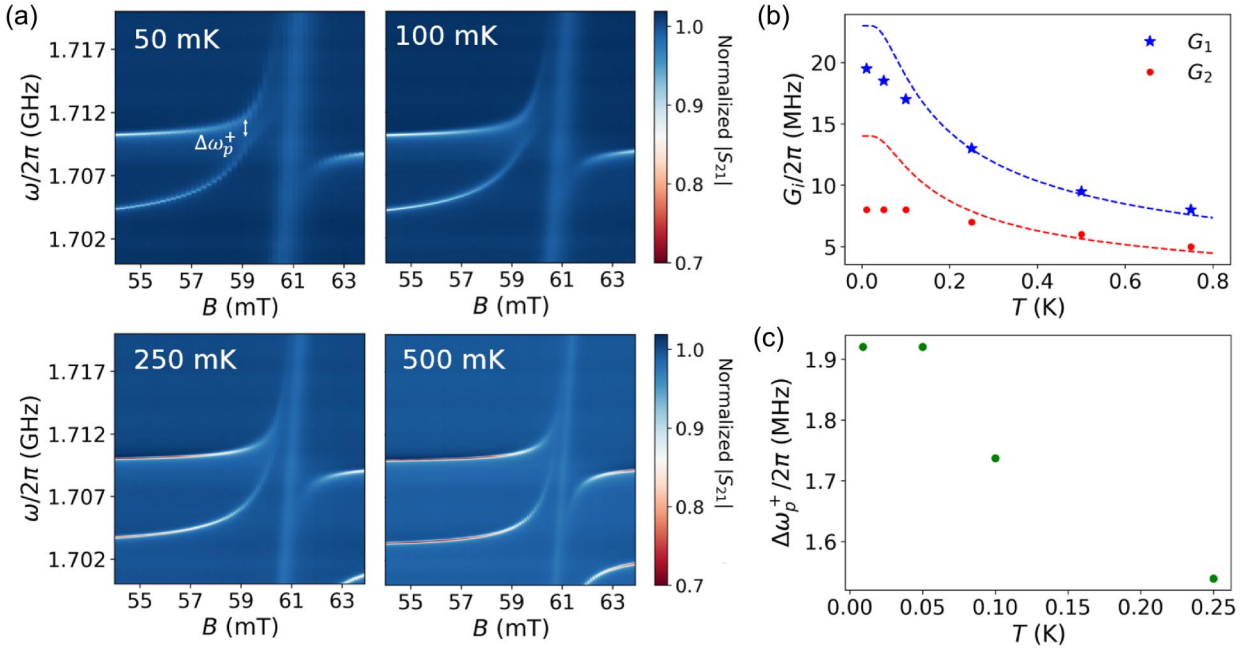


FIG. 17. (a) $2D$ transmission plots near the LER-1 and LER-2 resonances measured at different temperatures for a $-50$ dBm input power, equivalent to photon numbers $n \sim 5.5 \times 10^9$ for LER-1, $n \sim 5.06 \times 10^{10}$ for LER-2. (b) Temperature dependence of the collective coupling of each spin sample to photon modes of its host LER ($G_1$ and $G_2$ for LER-1 and LER-2, respectively). The lines are least-squares fits based on Eq. (B1), which describes the dependence of $G_i$ on spin polarization. (c) Temperature dependence of the splitting $\Delta\omega_p^+$ between the two upper polariton branches, which characterizes the remote polariton-polariton coupling. Notice that, as shown in (a), the avoided level crossing between these polariton branches shifts to higher magnetic fields as $T$ increases. At $T = 500$ mK the anticrossing is no longer detectable.

akin to increasing the effective spin temperature, as will be described in the next section.

### 3. Temperature dependence of spin-photon and polariton-polariton couplings

The effective interaction between the spins and their host LERs depends on the population of the spin-up and spin-down states, thus it is also affected by temperature. Increasing $T$ reduces the spin polarization at any magnetic field, leading to a decrease in $G_i$ given by the following expression:

$$G_i(T) = G_i(0)\sqrt{\tanh\left(\frac{g\mu_B BS}{k_B T}\right)}. \tag{B1}$$

Figure 17(a) shows microwave transmission data measured for the coupled LER-1 and LER-2 pair at four different temperatures. Both the local spin-photon coupling and the mutual polariton-polariton coupling depend on $T$. The decrease in $G_i$ with increasing $T$, shown in Fig. 17(b), also modifies the relative detuning between the two polariton branches, shifting the polariton-polariton anticrossing toward higher $B$. In addition, the gap $\Delta\omega_p^+$, shown in Fig. 17(c), gets reduced until it becomes undetectable for $T \geq 500$ mK. The fact that, as shown in Fig. 17(b), the dependence of $G_i$ with $T$ is weaker than that predicted by Eq. (B1) suggests a non-perfect thermalization of the samples, in particular that of Tripak$^-$, below 100 mK or the influence of weak antiferromagnetic interactions between different free radicals, which is likely in concentrated samples [51].

## APPENDIX C: TIME-RESOLVED PUMP-PROBE EXPERIMENTS

This section describes the results of pump-probe experiments that explore three scenarios, corresponding to excitations of different nature: pure photons, hybrid spin-photon polaritons and pure spins.

### 1. Photon-photon readout experiments

At $B = 0$ the excitations of two mutually detuned and coupled LERs are photons localized on either of them. Since the two systems are purely harmonic, changes in the photon population of one LER should not generate any

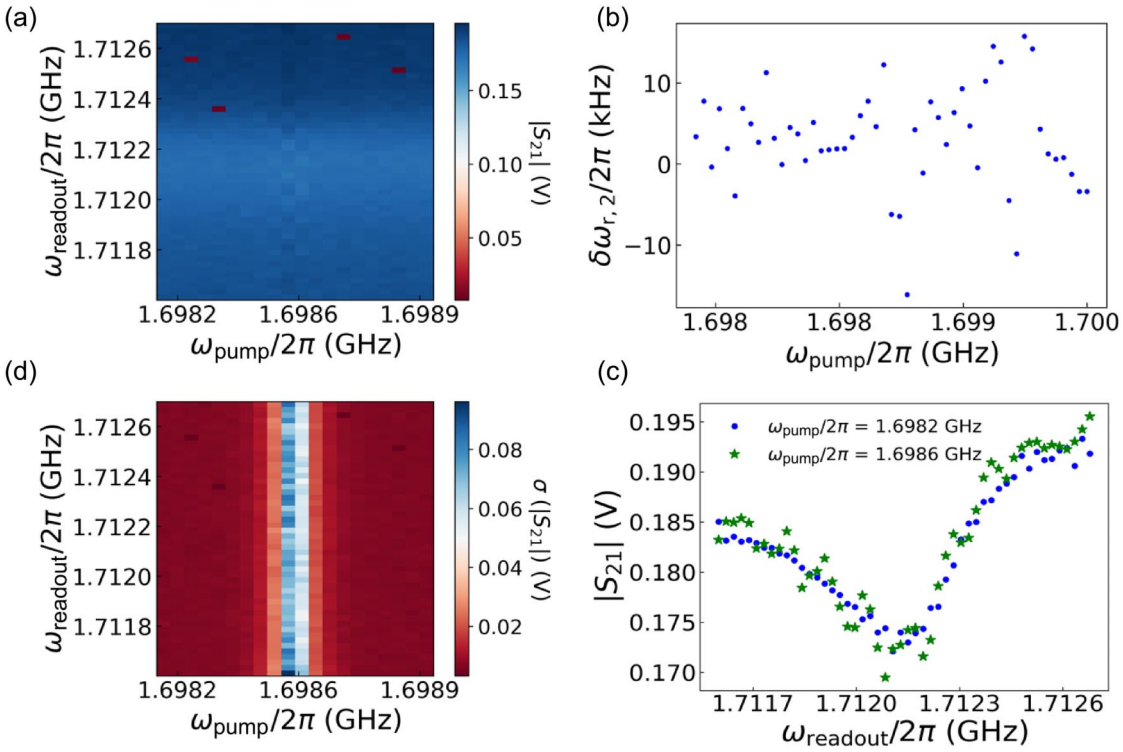


FIG. 18. Pump-probe photon-photon experiments performed at $B = 0$ on LER-1 and LER-2. (a) $2D$ color plot of the microwave transmission measured near $\omega_{r,2}$ after pumping at frequencies close to $\omega_{r,1}$. (b) Dependence of the LER-2 frequency shift $\delta\omega_{r,2}$ on the pumping frequency. (c) $S_{21}$ spectra extracted from the data in panel (a) at two different pump frequencies, being either far from ($\omega_{pump}/2\pi = 1.6982$ GHz) or close to ($\omega_{pump}/2\pi = 1.6986$ GHz) resonance with LER-1. In the latter case, fluctuations show up in the transmitted signal. These are associated with off-resonant excitation of LER-2 by microwave photons absorbed and then re-emitted by LER-1. (d) $2D$ color plot of the standard deviation of the microwave transmission data shown in (a). This quantity becomes maximum when the pump frequency gets close to $\omega_{r,1}$, confirming the onset of enhanced transmission fluctuations.

shift in the resonance frequency of the other one. The experiments were performed on the pair formed by LER-1 and LER-2. Illustrative results of exciting LER-1 and reading out the frequency changes in LER-2 are shown in Figs. 18(a) and 18(b). No noticeable shift in $\omega_{r,2}$ is observed. However, the microwave transmission shows enhanced fluctuations when the pump frequency matches $\omega_{r,1}$ [Fig. 18(c)], which become more noticeable if the transmission standard deviation is plotted, as shown in Fig. 18(d). A plausible explanation of this effect is as follows. When $\omega_{pump} \simeq \omega_{r,1}$, LER-1 gets charged and then it starts decaying as soon as the pumping pulse ends. Some of the emitted photons reach LER-2 through their common readout transmission line. However, since $\omega_{r,2} \neq \omega_{r,1}$, the excitation of LER-2 is incomplete and, besides, it oscillates with $\omega_{pump} - \omega_{r,2}$, which reflects itself in the transmission through the readout line.

### 2. Polariton-polariton readout experiments

We next consider pump-probe experiments performed on the same pair formed by LER-1, coupled to $N \sim 5 \times 10^{14}$ PTMr molecules, and LER-2, coupled to $N \sim 5 \times 10^{14}$ Tripak$^-$ molecules, at $B = 54$ mT and at $B = 64$ mT, when the spins are still relatively far from resonance with either LER [see Fig. 14(a)]. Therefore, since $(\omega_{r,2} - \omega_{r,1})/2\pi \simeq 7$ MHz is much larger than $\kappa_{1,2}/2\pi \sim 1$ MHz, the upper polaritons consist mainly of photons localized at either LER-1 or LER-2. However, contrary to what happens at $B = 0$, the local spin-photon couplings $G_1$ and $G_2$ do still confer to them a tiny spin component and make their frequencies, $\omega^+_{p,1}$ and $\omega^+_{p,2}$, depend on $B$. The excitation of, say, the upper LER-1 polariton induces then a local spin polarization change that, via the capacitive coupling $\kappa_{1,2}$, must generate a shift in the frequency $\omega^+_p$ of the upper LER-2 polariton.

An example of this shift is shown in Fig. 19(a), which gives the LER-2 resonance recorded at $B = 54$ mT before ("reference" data) and after the resonant excitation of LER-1 by a 50 μs long $\sim -7$ dBm squared pump pulse. The readout is performed by sending a train of one hundred 20 μs long pulses with frequencies around $\omega^+_{p,2}$. The results show a neat shift in $\omega^+_{p,2}$ relative to the reference data. The negative sign of $\delta\omega^+_{p,2}$ is due to the negative detuning of the spins with respect to LER-1 [i.e., $\Omega_{S,1} < \omega^+_{p,1}$, see Fig. 14(a)]. Data measured at $B = 64$ mT, using the same protocol at the corresponding polariton frequencies, show instead a positive $\delta\omega^+_{p,2}$ [Fig. 19(b)] because then $\Omega_{S,1} > \omega^+_{p,1}$.

As discussed in Appendix C 2 above, the roles of the two polaritons can be reversed. Then, we can also use polaritons from LER-1 to readout polariton excitations at LER-2 and, by varying the excitation frequency, obtain spectroscopy information of both polaritonic branches. Results obtained at $B = 54$ mT (leading to negative

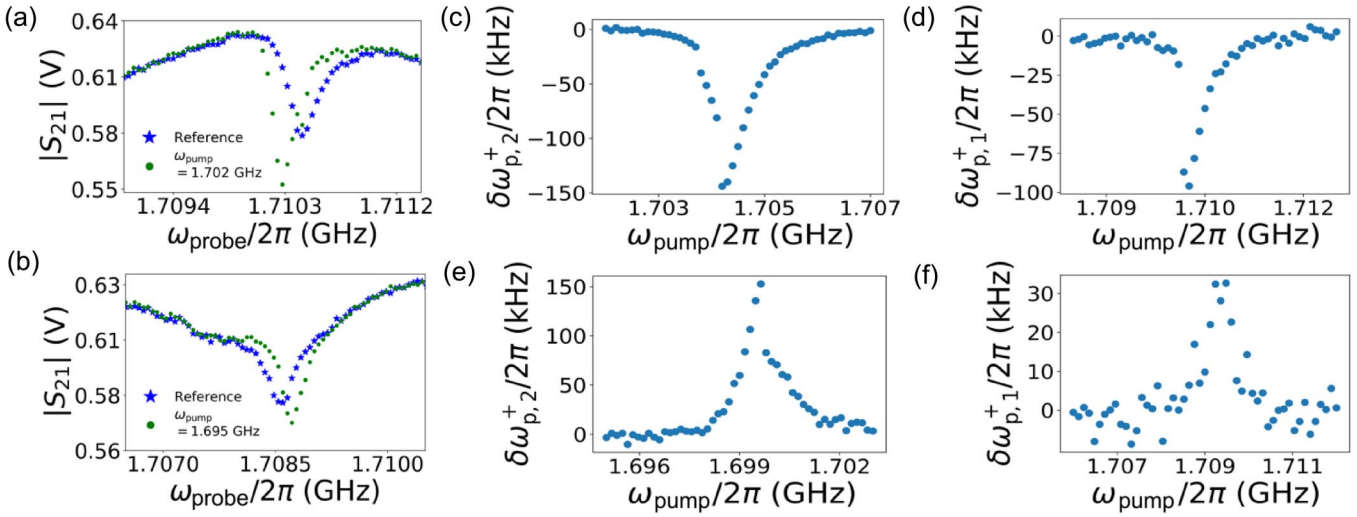


FIG. 19. Polariton-polariton readout measurements performed on the coupled LER-1 (coupled to $N \sim 5 \times 10^{14}$ PTMr spins) and LER-2 (coupled to $N \sim 5 \times 10^{14}$ Tripak$^-$ free radical molecules). Panels (a),(b) show the LER-2 upper polariton resonance measured at $B = 54$ mT and $B = 64$ mT, respectively, after the resonant excitation of the LER-1 upper polariton, compared to the reference data (measured without any previous excitation pulse). Panels (c),(d) show spectra of the LER-1 and the LER-2 upper polaritons, respectively, measured at $B = 54$ mT using the frequency shift $\delta\omega^+_{p,j}$, with $j = 2, 1$, respectively, of the other polariton as a probe. The polariton linewidths derived from these data are, approximately, $\kappa_{p,1}/2\pi \simeq 0.73$ MHz and $\kappa_{p,2}/2\pi \simeq 0.34$ MHz. Panels (e),(f) are the same as panels in (c),(d), respectively, for $B = 64$ mT. Notice the change in the sign of $\delta\omega^+_{p,j}$. The polariton linewidths at this field are $\kappa_{p,1}/2\pi \simeq 1.2$ MHz and $\kappa_{p,2}/2\pi \simeq 0.68$ MHz.

frequency shifts) are shown in Figs. 19(c) and 19(d), whereas data measured at $B = 64$ mT (leading to positive frequency shifts) are shown in Figs. 19(e) and 19(f). These results confirm also that the polariton linewidth $\kappa_{p,i}$ depends on $G_i$ and on magnetic field, which combine to determine the degree of spin-photon hybridization.

### 3. Spin readout and relaxation measurement

Finally, we consider the more conventional spin readout experiments, in which spin excitations are detected via the shift in the frequency of their host LER. Therefore, these experiments do not involve any nonlocal interaction, but are driven by the local spin photon couplings $G_1$ and $G_2$. Experiments were performed for LER-1 and LER-2 at $B = 66$ mT, using the same protocol described above for the "polariton-polariton" experiments. Only, here the excitation frequency $\sim\Omega_{S,i}$ and the readout is performed by recording the resonance of the same LER-$i$. These experiments allow estimating the spin relaxation time $T_1$ of both samples (PTMr and Tripak$^-$). To this end, we measure the resonance shift for increasing delay times $t$ between the pump and readout pulses. The results are shown in Fig. 20.

The decay of $\delta\omega_{\mathrm{r},i}$ with increasing $t$ is non exponential, likely reflecting a distribution in $T_1$ values associated with significant spin-spin interactions in these, quite concentrated, samples. In order to estimate $T_1$, we fit the experimental data using a stretched exponential function:

$$\delta\omega_{\mathrm{r},i}(t) = \delta\omega_{\mathrm{r},i}(0)e^{-(t/T_1)^x}, \tag{C1}$$

where the exponent $x \simeq 0.3$ accounts for the distribution in relaxation times. We find $T_1 \simeq 0.2$ s for PTMr and $T_1 \simeq 0.024$ s for Tripak$^-$.

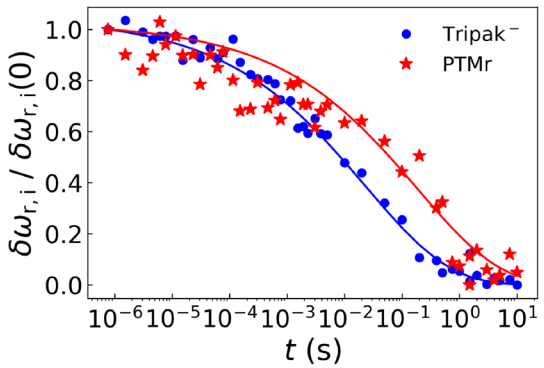


FIG. 20. Decay of the resonance frequency shift generated by the resonant spin excitation of PTMr (coupled to LER-1) and Tripak$^-$ (coupled to LER-2) spins at $B = 66$ mT. The solid lines are least-squares fits based on a stretched exponential [Eq. (C1)] with the parameters given in the text.

## APPENDIX D: THEORY: POLARITON-POLARITON COUPLING AND ANALYSIS OF MICROWAVE TRANSMISSION

### 1. Theoretical model: Hybrid modules and their coupling

In this section, we present a theoretical framework that describes the interactions within a LER-spin ensemble hybrid system, its energies and wave functions, and how these are modified by its coupling to another hybrid module and by external parameters, mainly the magnetic field. The system under study is sketched in Fig. 5(a). It includes a LER pair, hereafter labeled generically as LER-1 and LER-2, with bare resonance frequencies $\omega_{\mathrm{r},1}$ and $\omega_{\mathrm{r},2}$. Each LER can host a different spin ensemble, giving rise to local collective spin-photon couplings $G_1$ and $G_2$. We also denote by $\kappa_{1,2}$ the mutual capacitive coupling between them (see Fig. 7). The terms that give rise to dissipation, in particular the couplings of the two LERs and of the spins to the readout transmission line, will be considered in Appendix D 3 below. The Hamiltonian describing the system is then given by

$$\mathcal{H} = \mathcal{H}_0 + \mathcal{H}_{\mathrm{sr}} + \mathcal{H}_{\mathrm{rr}}, \tag{D1}$$

where

$$\mathcal{H}_0 = \sum_{j=1}^{2} (\omega_{\mathrm{r},j} a_j^\dagger a_j + \Omega_{S,j} S_j^z), \tag{D2}$$

describes the isolated resonator and spin systems,

$$\mathcal{H}_{\mathrm{sr}} = \sum_{j=1}^{2} G_j (a_j S_j^+ + a_j^\dagger S_j^-) \tag{D3}$$

describes the local spin-resonator interaction and

$$\mathcal{H}_{\mathrm{rr}} = \kappa_{1,2}(a_1^\dagger a_2 + a_2^\dagger a_1), \tag{D4}$$

accounts for the mutual coupling between two resonators within a pair.

In the expressions above, $a_j$ and $a_j^\dagger$ represent the photon annihilation and creation operators, respectively, in each cavity $j = 1, 2$, $S_j^\alpha$, with $\alpha = z, +, -$, represent conventional spin-1/2 operators, and the spin resonance frequency is related to the magnetic field through $\Omega_{S,j} = g_j \mu_{\mathrm{B}} B$, in agreement with the experiments shown in Fig. 10.

Before describing situations characterized by a finite interaction between the two LERs, given by Eq. (D4), we first consider the limit of vanishing $\kappa_{1,2}$, which allows introducing mathematically the spin polaritons. These are single light and matter excitations that arise as eigenstates of the Hamiltonian formed by $\mathcal{H}_0 + \mathcal{H}_{\mathrm{sr}}$. In order to write

these eigenstates down, let us first define our basis as $\{|n_1, m_1^z, n_2, m_2^z\rangle\}$ where $n_j$ indicates the number of photons in LER $j$ (here, either 0 or 1) and $m_j^z = \{\uparrow, \downarrow\}$ is the spin polarization along its quantization axis $z$. Let $|\downarrow\rangle$ be the ground state of the spin subsystem. Now, the polaritons of module $j \neq i$ are defined by the following states

$$|p_j^+\rangle = \left(\sin\frac{\theta_j}{2}\,|0,\uparrow\rangle_j + \cos\frac{\theta_j}{2}\,|1,\downarrow\rangle_j\right)|0,\downarrow\rangle_i, \quad \text{(D5a)}$$

$$|p_j^-\rangle = \left(\cos\frac{\theta_j}{2}\,|0,\uparrow\rangle_j - \sin\frac{\theta_j}{2}\,|1,\downarrow\rangle_j\right)|0,\downarrow\rangle_i, \quad \text{(D5b)}$$

and similarly for the polaritons of module $i$. Here, $\theta_j = \tan^{-1}(2G_j/\Delta_j)$ and $\Delta_j = (\Omega_{S,j} - \omega_{r,j})$ are the usual parameters that characterize the spin-photon hybridization within a Jaynes-Cummings model [65]. The maximum spin-photon hybridization occurs when $\theta_j = \pi/2$, which corresponds to the resonance condition $\Delta_j = 0$.

Although we refer here to the Jaynes-Cummings model, the canonical microscopic description is the Tavis-Cummings model [66], since we are dealing with spin ensembles. In the single-excitation manifold, however, the symmetric (bright) collective mode of each ensemble is exactly equivalent to an effective spin-1/2 coupled to its cavity with the collective strength $G = \propto \sqrt{N}$. The single-excitation spectra, eigenstates, and correlations are therefore identical in the two descriptions, and we adopt the compact Jaynes-Cummings-like notation of Eqs. (D1)–(D5), with $G_j$ denoting the collective coupling of each ensemble to its cavity.

It is worth clarifying at this point how this single-excitation description relates to the experiments. The transmission spectra reported here are measured with a number of photons in the cavity that is much larger than one, but with excitation fractions $n/N \lesssim 10^{-4}$ that remain very small (see Appendix B 2). In this weakly excited regime, each spin ensemble is accurately described by a bosonic collective mode obtained through the Holstein-Primakoff transformation, and the driven response follows the linearized input-output treatment of Appendix D 2. Since both descriptions involve the same bright collective mode and the same collective coupling $G$, they predict the same mode frequencies and linewidths, which is what allows the calculated single-excitation spectra to be compared directly with the measured transmission. The parameters derived from the many-photon driven measurements allow then extracting information on single-excitation eigenstates, even though the latter are not directly probed in these experiments.

In the following sections, we consider systems with increasing levels of complexity, which correspond to the two experimental situations described in Sec. III. The first includes two coupled LERs but just one spin ensemble that interacts with only one of them. Then, we will discuss the more general scenario where each LER hosts a different spin ensemble. These theoretical results complement the experimental ones and show how properties of the system, as the eigenstate wave functions or the photon entanglement, can be inferred from the model using parameters extracted from spectroscopy data.

### a. First model scenario: One spin ensemble and 2 LERs

For clarity, we begin by studying the case where only one of the LERs hosts a coupled spin ensemble, corresponding to the setup shown in Fig. 3(a). In this case, we set $\Omega_{S,2} = 0$ in Eq. (D2) and $G_2 = 0$ in Eq. (D3) and obtain the other parameters from experiment. Figure 21 shows the results of calculations that match the most salient features found in the experiments. The main finding is the remote coupling $G_{1,2}$ of the spin ensemble to the nominally empty LER, labeled in these calculations as LER-2, which is mediated by the capacitive interaction $\kappa_{1,2}$. Our aim here is to derive an expression for $G_{1,2}$ that shows how this indirect coupling depends on the circuit design and then also provide information about the system energies and wave functions as a function of $B$.

In order to carry out these calculations and gain some intuition on the results, we will start from the unperturbed Hamiltonian $\mathcal{H}_0$ [Eq. (D2)], whose energy eigenstates are trivial localized photon and spin excitations [Fig. 21(a)], and proceed by adding the different interactions. When $\kappa_{1,2} \neq 0$ [Figs. 21(b) and 21(c)] it is convenient to work in a basis defined by the normal modes $\mu = +, -$ of the coupled LER pair, described by new creation and annihilation operators $b_\mu^\dagger$ and $b_\mu$, respectively. In this new basis, the Hamiltonian reads

$$\mathcal{H} = \Omega_{S,1} S_1^z + \sum_{\mu=+,-} \tilde{\omega}_\mu b_\mu^\dagger b_\mu + \sum_{\mu=+,-} \tilde{G}_{1,\mu}(b_\mu S_1^+ + b_\mu^\dagger S_1^-), \quad \text{(D6)}$$

with $\tilde{\omega}_\pm = \frac{1}{2}(\omega_{r1} + \omega_{r2} \pm \sqrt{(\Delta\omega_r)^2 + 4\kappa_{1,2}^2})$ and $\Delta\omega_r = \omega_{r2} - \omega_{r1}$. The normal mode operators $b_\mu$ and the single LER ones $a_j$ are related by

$$b_+ = \cos\frac{\phi}{2} a_1 + \sin\frac{\phi}{2} a_2, \quad \text{(D7a)}$$

$$b_- = -\sin\frac{\phi}{2} a_1 + \cos\frac{\phi}{2} a_2, \quad \text{(D7b)}$$

where $\phi = \tan^{-1}(2\kappa_{1,2}/\Delta\omega_r)$ is a mixing angle that parametrizes the degree of localization of the two normal modes. Since the eigenstates $|\psi_j\rangle$ of (D6) need not be localized on either LER, from now on we will label them in order of increasing energy [cf. Fig. 21(c)].

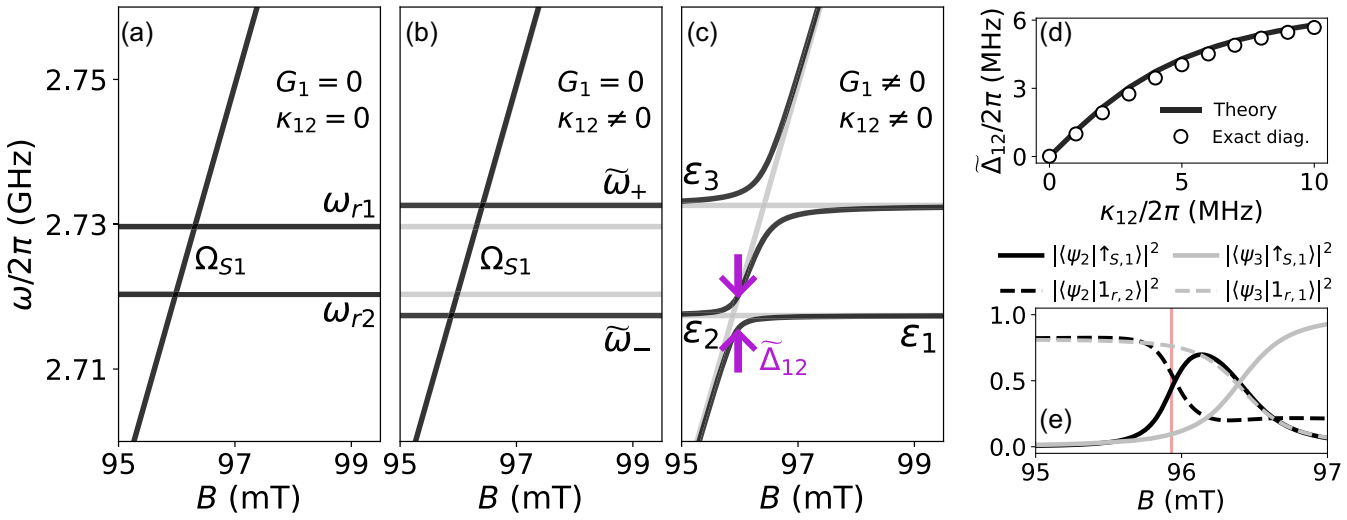


FIG. 21. Eigenvalues of the Hamiltonian (D6) that describes two coupled LERs, only one of them (in this case LER-1, with the highest resonance frequency $\omega_{r,1}$) being coupled to a spin ensemble. Panels (a)–(c) display the evolution of the system energies from the uncoupled limit to the fully interacting scenario. Light gray lines in (b),(c) show the levels in (a),(b), respectively, i.e., before switching on a relevant interaction to better visualize its effect. Panel (d) illustrates how the experimentally observed gap $\tilde{\Delta}_{1,2}$ between the two lower polariton branches depends on the inter-cavity coupling parameter $\kappa_{1,2}$. The open circles are calculated by exact diagonalization of the Hamiltonian (D6) and the solid line follows from Eqs. (D9) and (D10). Panel (e) shows the probabilities of eigenstates $|\psi_2\rangle$ (with energy $\epsilon_2$ in panel (c)) and $|\psi_3\rangle$ (with energy $\epsilon_3$) in the single-excitation subspace basis for both LERs and the spin. The solid vertical red line marks the anticrossing shown by the purple arrows in panel (c). The values chosen for the model parameters are $\omega_{r1}/2\pi = 2.730$ GHz, $\omega_{r2}/2\pi = 2.720$ GHz, $G_1/2\pi = 5.4$ MHz, $\kappa_{1,2}/2\pi = 6.49$ MHz.

It follows from Eq. (D6) that the spin ensemble, even though localized on LER-1, now couples directly to both normal modes via $\tilde{G}_{1,\pm}$. These coupling rates relate to the original $G_1$ as follows

$$\tilde{G}_{1,+} = G_1 \cos\frac{\phi}{2}, \tag{D8a}$$

$$\tilde{G}_{1,-} = -G_1 \sin\frac{\phi}{2} \tag{D8b}$$

and give rise to avoided level crossings when the spin frequency is brought into resonance to any of the normal modes, as shown in Fig. 21(c). The coupling $G_{1,2}$ found experimentally (Fig. 3) is then given by $\tilde{G}_{1,-}$. Using Eq. (D8b) and the fact that the $b_-$ normal mode is still predominantly localized at LER-2, we can approximate

$$G_{1,2} \simeq G_{1,-} = \frac{G_1}{\sqrt{2}}\sqrt{1 - \frac{\Delta\omega_r}{\sqrt{(\Delta\omega_r)^2 + 4\kappa_{1,2}^2}}}, \tag{D9}$$

where we have omitted the negative sign in Eq. (D8b) since it is not relevant for the discussion that follows.

The remote coupling $G_{1,2}$ then arises from the local spin-photon interaction $G_1$ and the delocalization of the LER pair normal modes that is generated by $\kappa_{1,2}$. When $\kappa_{1,2} \gg \Delta\omega_r$, $G_{1,2} \to G_1/\sqrt{2}$. This result is intuitive considering that, in this limit, LER excitations are fully delocalized symmetric and antisymmetric normal modes, thus the spin ensemble couples identically to both of them. As mentioned above, $G_{1,2}$ leads to the gap $\tilde{\Delta}_{1,2}$ that opens between the energies $\epsilon_1$ and $\epsilon_2$ of eigenstates $\psi_1$ and $\psi_2$ [Fig. 21(c)]. To a good approximation, the relation between $G_{1,2}$ and $\tilde{\Delta}_{1,2}$ is simply given by

$$\tilde{\Delta}_{1,2} = \min(\epsilon_2 - \epsilon_1) \approx 2G_{1,2}. \tag{D10}$$

This relation is fulfilled over a wide range of $\kappa_{1,2}$ values, as shown by Fig. 21(d), which compares the actual gap obtained by the exact diagonalization of the full Hamiltonian (D6) to that derived from Eqs. (D9) and (D10). From a practical point of view, Eq. (D10) provides a simple method to estimate the remote coupling constant $G_{1,2}$ and, from it, $\kappa_{1,2}$ via Eq. (D9), using microwave transmission data as it is done with the data of Fig. 3.

It is also of interest to estimate the magnetic field at which the anticrossing occurs. In essence, it arises from the resonance, induced by $B$, between the lower polariton generated at LER-1 and the $b_-$ mode that is closer to LER-2. Based on Hamiltonian (D6), we can restrict our analysis to the single-excitation subspace and treat the coupling $\tilde{G}_{1,-}$ as a perturbation. Consequently, we re-diagonalize the block corresponding to the symmetric photonic mode $b_+$ and the spin ensemble, which are

coupled via $\tilde{G}_{1,+}$. The resulting LER-1 polariton "pseudo-eigenenergies" are then approximately given by

$$\tilde{\epsilon}_{\pm} = \frac{1}{2}\left(\Omega_{S,1} + \tilde{\omega}_{+} \pm \sqrt{(\Omega_{S,1} - \tilde{\omega}_{+})^2 + 4\tilde{G}_{1,+}^2}\right). \tag{D11}$$

Since $\tilde{\omega}_{-} < \tilde{\omega}_{+}$, the LER-1 polariton branch that intersects with $\tilde{\omega}_{-}$ is $\tilde{\epsilon}_{-}$. The intersection occurs when $\tilde{\epsilon}_{-}(\Omega_{S,1}) = \tilde{\omega}_{-}$ that leads to

$$\Omega_{S,1} = g_1 \mu_B B \approx \tilde{\omega}_{-} + \frac{\tilde{G}_{1,+}^2}{\tilde{\omega}_{+} - \tilde{\omega}_{-}} \tag{D12}$$

provided that $(\Omega_{S,1} - \tilde{\omega}_{+}) \gg \tilde{G}_{1,+}$. The spin-photon hybridization at LER-1 then shifts the resonance field from that of the bare spin, defined by $\Omega_{S,1} = \tilde{\omega}_{-}$. Besides, this shift decreases as either the detuning $\Delta\omega_r$ between the two LERs or their mutual coupling $\kappa_{1,2}$ increases. This can be understood as a result of the LER-1 lower polariton branch becoming progressively closer to a pure spin excitation at its crossing with $b_{-}$, as the two modes become further separated in energy.

As a somewhat related effect, we next consider the entanglement between LER-1 and LER-2 photons in each eigenstate of the system $|\psi_j\rangle$ and how it evolves as a function of magnetic field. Here, we quantify this entanglement by the negativity of the reduced two-photon state $\rho_j$ across the LER-1 | LER-2 partition, which is an entanglement monotone [67] and is defined as follows

$$\mathcal{N}(\rho_j) = \frac{||\rho_j^{\Gamma_{\text{LER-1}}}||_1 - 1}{2} = \left|\sum_{\lambda_i<0}\lambda_i\right|, \tag{D13}$$

where $\rho_j^{\Gamma_{\text{LER-1}}}$ is the partial transpose of the reduced density matrix $\rho_j$ with respect to subsystem LER-1. The reduced density matrix $\rho_j$ is that of the bipartite subsystem formed by the two photonic modes, obtained from the full eigenstate by tracing out the spin ensemble, $\rho_j = \text{Tr}_{S1}(|\psi_j\rangle\langle\psi_j|)$. This trace reduces the original tripartite system (LER-1, LER-2 and spin ensemble S1) to a bipartite one (LER-1, LER-2) on which the negativity can be defined.

The negativity of Eq. (D13), shown in Fig. 22 and evaluated on the model eigenstates with $G_1$ and $\kappa_{1,2}$ fixed to their spectroscopically determined values, is an inferred property of the polariton eigenstates rather than a directly measured quantity. Within this framework, the results reveal that the hybrid character of the lower LER-1 polariton, generated by the local spin-photon coupling $G_1$, leads to a local entanglement maximum near the anticrossing of this polariton with mode $b_{-}$, which is localized close to LER-2. As discussed above, the hybridization introduces some photonic character into the polariton branch, which then enhances the photon entanglement with respect to that given solely by $\kappa_{1,2}$ (gray lines in Fig. 22). The relative intensity of this effect diminishes as $\kappa_{1,2}$ increases, and can thus be tuned by circuit design. The higher the baseline photon entanglement, the smaller the spin contribution, provided the system is not in the regime where $G_1 \gg \kappa_{1,2}$. Evaluated with parameters determined experimentally for the LER-9, LER-10 pair (Fig. 3), which correspond to a relatively large $\kappa_{1,2} \simeq 0.7\ \Delta\omega_r$, the inferred spin-induced entanglement is quite small. The next section covers a different situation in a different parameter regime.

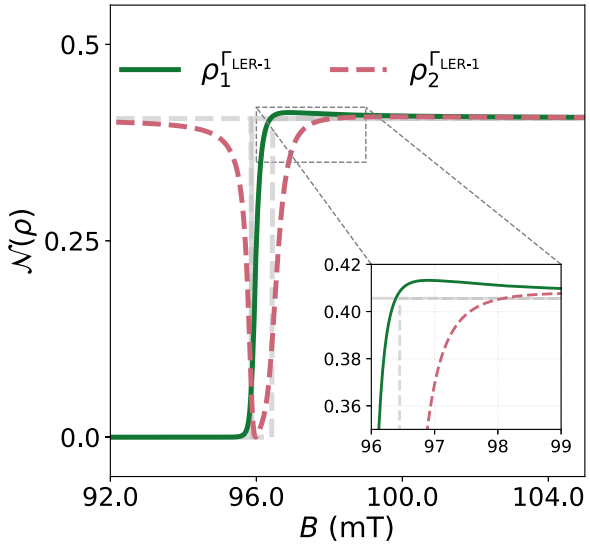


FIG. 22. Entanglement between LER-1 and LER-2 photons as a function of magnetic field. It is computed as the negativity of LER-1, defined by Eq. (D13), in eigenstates $|\psi_1\rangle$ and $|\psi_2\rangle$ of the Hamiltonian (D6). The parameters considered are those used in Fig. 21. The light gray lines show the negativity calculated for $G_1 = 0$, i.e., when the photons are decoupled from the spins. The inset shows a close-up of the region close to the anticrossing between $\psi_1$ and $\psi_2$ in Fig. 21. A maximum entanglement between both photons then occurs for $G_1 \neq 0$ near the anticrossing between the LER-1 lower polariton and the quasi LER-2 mode $b_{-}$ [see Fig. 21(c)].

### b. Second model scenario: Two spin ensembles and two LERs

We next theoretically analyze the behavior of a system where both LERs host spin ensembles. The two ensembles possess different resonance frequencies $\Omega_{S,j}$ due to their different $g$-factors. Moreover, each sample also presents a different spin-photon coupling $G_j$ to its host LER. The parameters considered here correspond to those extracted from the experiment described in Fig. 4. The main experimental phenomenon we aim to characterize is the anticrossing occurring between the two upper polariton branches.

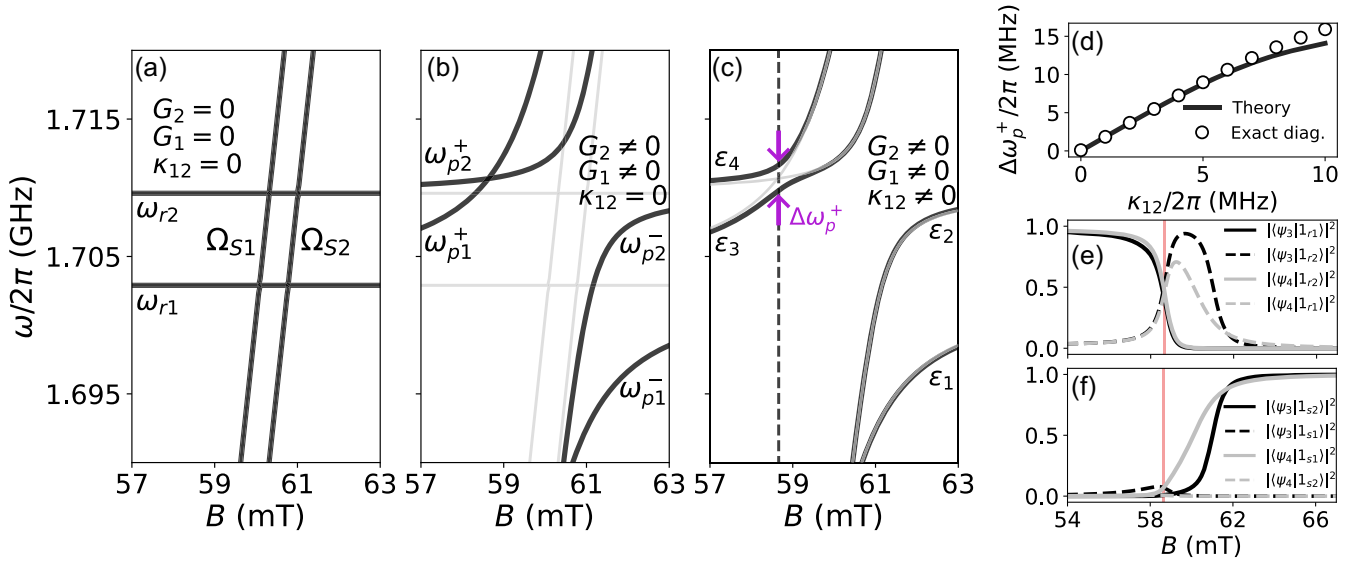


FIG. 23. Eigenvalues of the Hamiltonian (D1) that describes two coupled LERs, each of them coupled to a different spin ensemble. Panels (a)–(c) display the evolution of the system energies from the fully uncoupled limit to the fully interacting scenario (corresponding to the experimental configuration shown in Fig. 4). Panel (d) illustrates the relationship between the polariton-polariton gap $\Delta\omega_{\rm p}^+$ separating the two upper polariton branches and the inter-cavity coupling parameter $\kappa_{1,2}$. The circles are obtained by exact diagonalization of the full Hamiltonian (D1) and the solid line follows from Eq. (D14). Finally, panels (e),(f) show the probabilities that eigenstates $|\psi_3\rangle$ and $|\psi_4\rangle$ have in the single-excitation subspace basis for the two LERs [panel (e)] and the two spin ensembles [panel (f)]. The vertical red line indicates the anticrossing point marked by a black dashed line in panel (c). The parameters used in these simulations are $\omega_{r1} = 1.7029$ GHz, $\omega_{r2} = 1.7096$ GHz, $G_1 = 19.5$ MHz, $G_2 = 8.5$ MHz and $\kappa_{1,2} = 1.06$ MHz.

Like in the previous case, the eigenstates and the frequencies of the two coupled hybrid spin-cavity modules have been calculated by diagonalization of Hamiltonian (D1). The results are shown in Fig. 23, which illustrates how they evolve as the different interactions are "switched on." The anticrossing, characterized by the $\Delta\omega_{\rm p}^+$ gap in Fig. 23(c), reflects the interaction between two hybrid spin-photon excitations, each arising from one of the two spin-LER subsystems. In this scenario, the capacitive photon-photon coupling $\kappa_{1,2}$ therefore couples remote polaritons.

To understand the relationship between the gap and $\kappa_{1,2}$, we revisit the model defined by Eq. (D1), but now with $\Omega_{S,2}$ and $G_2 \neq 0$. A further distinction from the previous case is that we now proceed by first diagonalizing the blocks corresponding to the spin-photon interaction within each LER, giving rise to polariton states $|p_j^{\pm}\rangle$, $j = 1, 2$, defined by Eqs. (D5a) and (D5b) with frequencies $\omega_{\rm p}^{\pm}$ shown in Fig. 23(b). Then, we treat the inter-LER coupling as a perturbation. From those states, we can define the effective coupling parameter between the two upper, symmetric, polaritons as the matrix element of the perturbation $\mathcal{H}_{\rm sr}$ between them, i.e., $J_{1,2}^+ \equiv \langle p_1^+|\mathcal{H}_{\rm sr}|p_2^+\rangle$.

The gap $\Delta\omega_{\rm p}^+$ between the frequencies of these polariton branches can then be approximated by

$$\Delta\omega_{\rm p}^+ \simeq 2J_{1,2}^+ = 2\kappa_{1,2}\cos\frac{\theta_1}{2}\cos\frac{\theta_2}{2}. \tag{D14}$$

The gap scales as $\kappa_{1,2}$, reflecting the dominant photonic nature of the polaritons, but depends also on their spin components, defined by $\theta_1$ and $\theta_2$ [Eqs. (D5a) and (D5b)], which are induced by the local spin-photon interactions $G_1$ and $G_2$. In fact, it is their spin component that renders them sensitive to the magnetic field and ultimately drives the crossing. Note that $J_{1,2}^+$ is not purely proportional to $\kappa_{1,2}$, and neither is $\Delta\omega_{\rm p}^+$ as Fig. 23(d) shows, since $\kappa_{1,2}$ also determines the magnetic field at which the two polariton branches cross. In this case, the approximation breaks down earlier than for Eq. (D10) due to the presence of additional interacting subsystems with non-negligible couplings.

The comparison between the theoretical polariton-polariton interaction and that determined experimentally (Figs. 4 and 14) deserves a cautious comment. In order to reduce the number of free parameters, the polariton frequencies, thus also $\Delta\omega_{\rm p}^+$ and the microwave transmission shown in Figs. 4(d), 4(f) and 5(c), have been evaluated by varying only the capacitive coupling $\kappa_{1,2}$. However, the influence that this coupling has on the system energies and wave functions depends on the actual detuning between the "bare" resonance frequencies of both LERs (i.e., the frequencies they would have for $\kappa_{1,2} = 0$), which, as mentioned above, are modified by the dielectric properties of the molecular deposits. The value of $\kappa_{1,2}$ needed to fit the data might therefore differ from that obtained from simulations of a "clean" circuit (see Fig. 7).

Accordingly, the value $\kappa_{1,2}/2\pi = 1.06$ MHz quoted here should be regarded as an effective fitting parameter, which also absorbs the residual uncertainty in the bare LER detuning $\Delta\omega_r$, rather than as an independent determination of the geometric capacitive coupling. The correlation between these two quantities can be made explicit: the LER normal-mode frequencies $\tilde{\omega}_\pm$ [Eq. (D6)], and therefore the polariton frequencies and the gap $\Delta\omega_p^+$, depend on them mainly through the combination $\sqrt{(\Delta\omega_r)^2 + 4\kappa_{1,2}^2}$. A larger $|\Delta\omega_r|$ is thus compensated by a smaller $\kappa_{1,2}$, and vice versa. Disentangling the two would require an independent measurement of the bare LER frequencies after the molecular deposition, which the present devices do not allow.

The combination of local and remote interactions leads to correlations between the spin and photon components, which are tuned by the magnetic field as it brings local polaritons in and out mutual resonance. This effect can be seen by looking at the polariton wave functions, i.e., to the probabilities that the exact eigenstates $|\psi_3\rangle$ and $|\psi_4\rangle$ (again sorted by energy) have in the basis of local single photon and single spin excitations. These probabilities are shown in panels (e) and (f) of Fig. 23, respectively. The vertical red line corresponds to the anticrossing marked as a dashed black line in panel (c). At this point, the two wave functions become maximally delocalized over the two LER photons. The different spin-photon couplings at each LER lead to asymmetric correlations between their photon excitations. For instance, panel (e) shows that the mode originating as LER-1 acquires significantly more LER-2 character than the converse. Interestingly, the mode originating as LER-2 exhibits less hybridization with LER-1 because it simultaneously transitions into a "spin-1" excitation. Here, the level crossings do not merely involve a predominantly photon-like eigenstate transitioning into a spin-like excitation, as in a conventional polariton. Rather, after the crossing, an eigenstate starting as a LER-$j$ photon transforms into an excitation of the spin ensemble $i$ located at the other LER-$i$. At the intermediate point, the wave functions exhibit nonzero amplitudes for all four subsystems.

To better understand this behavior and quantify the effective spin-spin interaction mediated by the circuit, we move to a basis different from that used in Eqs. (D5a) and (D5b). Specifically, we return to the photonic normal mode basis [cf. Eq. (D6)] and treat the spin-mode coupling as a perturbation. Thus, we now define

$$\mathcal{H}_0' = \sum_j \Omega_{Sj} S_j^z + \sum_{\mu=+,-} \tilde{\omega}_\mu b_\mu^\dagger b_\mu \tag{D15}$$

and

$$\tilde{V} = \sum_{j,\mu} \tilde{G}_{j,\mu} (b_\mu S_j^+ + b_\mu^\dagger S_j^-), \tag{D16}$$

where the normal mode operators $b_\pm$ have been defined in Eqs. (D7a) and (D7b), their couplings to spin-1 $\tilde{G}_{1,\pm}$ are those defined in Eqs. (D8a) and (D8b), and their couplings to spin-2 read

$$\tilde{G}_{2,+} = G_2 \sin\frac{\phi}{2}, \tag{D17a}$$

$$\tilde{G}_{2,-} = G_2 \cos\frac{\phi}{2}. \tag{D17b}$$

From here, it is possible to derive an effective Hamiltonian by applying a Schrieffer-Wolff transformation, defined by $\mathcal{H}_{\text{eff}} = e^{\mathcal{S}} \mathcal{H} e^{-\mathcal{S}}$ [68]. The operator $\mathcal{S}$ is such that the relation $\tilde{V} + [\mathcal{S}, \mathcal{H}_0'] = 0$ is fulfilled. After this transformation, the effective Hamiltonian reads

$$\mathcal{H}_{\text{eff}} = \mathcal{H}_0' + \frac{1}{2}[\mathcal{S}, \tilde{V}] + \frac{1}{3}[\mathcal{S}, [\mathcal{S}, \tilde{V}]] + \cdots \tag{D18}$$

For the present case, the anti-Hermitian operator $\mathcal{S}$ reads

$$\mathcal{S} = \sum_{j,\mu} \frac{\tilde{G}_{j,\mu}}{\tilde{\Delta}_{j,\mu}} (b_\mu S_j^+ - b_\mu^\dagger S_j^-), \tag{D19}$$

with $\tilde{\Delta}_{j,\mu} = \Omega_{S,j} - \tilde{\omega}_\mu$. In the resulting effective Hamiltonian, we are going to eliminate, up to first order in the expansion (D18), the interaction between the spins and the normal modes. This approximation will properly describe the system whenever $G_j \ll \tilde{\Delta}_{j,\mu}$, i.e., in the dispersive regime. If we stop the series (D18) at the second order, the effective Hamiltonian takes the form

$$\mathcal{H}_{\text{eff}} = \mathcal{H}_0' + \mathcal{H}_{\text{disp}} + \mathcal{H}_{\text{spin-spin}}. \tag{D20}$$

The first term, $\mathcal{H}_0'$, is just Eq. (D15), the second one,

$$\mathcal{H}_{\text{disp}} = \sum_{j,\mu} \frac{\tilde{G}_{j,\mu}^2}{\tilde{\Delta}_{j,\mu}} (2 b_\mu^\dagger b_\mu + 1) S_j^z, \tag{D21}$$

describes the usual dispersive effect that the coupling between the spins and the normal mode has on their frequencies, and the third and last term,

$$\mathcal{H}_{\text{spin-spin}} = \frac{J}{2}(S_1^+ S_2^- + S_1^- S_2^+), \tag{D22}$$

where $J = \sum_\mu \tilde{G}_{1,\mu} \tilde{G}_{2,\mu} (\tilde{\Delta}_{1\mu}^{-1} + \tilde{\Delta}_{2\mu}^{-1})$, describes an emerging spin-spin interaction. Note that $J \propto G_1 G_2 \kappa_{1,2}$ since it is a third-order process. The spin ensemble $j$ first couples to its host LER-$j$, via $G_j$, which in turn forms a hybrid mode with the adjacent resonator through $\kappa_{1,2}$, and then interacts with the distant spin ensemble, $i$, via $G_i$. It is important to emphasize that this analysis holds only in the dispersive

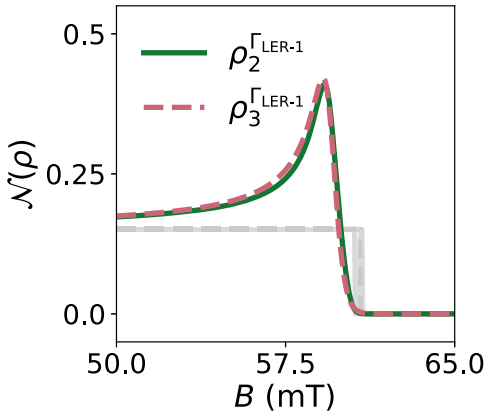


FIG. 24. Photon entanglement as a function of the external magnetic field computed as the negativity for the subsystem LER-1 according to Eq. (D13), after tracing out the spin degrees of freedom. The parameters considered are the same as in Fig. 23. The gray lines indicate the negativity evolution for the same eigenstates as the respective colored lines but in the case where $G_1 = G_2 = 0$.

regime where $G_j \ll \tilde{\Delta}_{j,\mu}$. To study the spin and photon hybridization near resonance, it is necessary to resort to the numerical diagonalization methods illustrated in Fig. 23.

Finally, we revisit the evolution of photon entanglement between the two cavities as a function of magnetic field, now in the presence of two spin ensembles. Applying the same analysis as in the previous scenario [the negativity of Eq. (D13) evaluated on the model eigenstates], Fig. 24 shows that this inferred entanglement is enhanced even further by the presence of the spins, becoming a factor 2 larger than the baseline entanglement of the cavities in the absence of spins. Once again, the spin ensembles act as local "tuning knobs" of the polariton frequencies, bringing them into resonance via their interaction with the magnetic field.

The theoretical results discussed in this and in the previous sections illustrate the possibilities that this modular polariton platform offers for controlling spin-spin and photon-photon correlations within a chip by tuning the magnetic field and other external parameters. Moreover, the range over which effective spin-spin interactions and the photon entanglement predicted by the model can be varied is set by the circuit design. Finally, this theoretical framework also provides the basis for interpreting the microwave transmission experiments reported in the previous sections. The corresponding methods are described below.

### 2. Input-output theory: Calculation of microwave transmission

The Hamiltonian and the mode spectrum underlying the arguments developed in this section so far can be tested experimentally by means of microwave transmission experiments, in which photons sent through a waveguide interact with the system, yielding direct information about its energy level spectrum. We stress that these measurements validate the Hamiltonian, the calculated mode spectrum and the parameters entering the model; the effective spin-spin interaction $J$ and the photon entanglement discussed above are predictions derived from that experimentally validated model, and not quantities directly determined from the transmission data. To describe these experiments, we employ standard input-output theory [69]. Starting from the Hamiltonian introduced in Eqs. (D1)–(D4), we map our spins onto harmonic oscillators via the Holstein-Primakoff transformation [70]. Then, each spin ensemble is characterized by its creation and annihilation operators, $c_j^\dagger$ and $c_j$, respectively. Solving for the time evolution of the expectation values of operators $a_j$, $a_j^\dagger$, $c_j$, and $c_j^\dagger$ by applying standard approximations, such as the rotating wave approximation, and focusing on the steady-state solution for a perturbative driving of amplitude $\alpha_{\text{in}}$, we arrive at

$$-i\alpha_{\text{in}}\begin{pmatrix}\sqrt{\gamma_{c1}}\,e^{i\phi_1}\\ \sqrt{\kappa_{c1}}\\ \sqrt{\kappa_{c2}}\\ \sqrt{\gamma_{c2}}\,e^{i\phi_2}\end{pmatrix} = \underbrace{\begin{pmatrix} i(\Omega_{S1}-\omega)+\gamma_1 & iG_1 & 0 & 0\\ iG_1 & i(\omega_{r1}-\omega)+\kappa_1 & i\kappa_{1,2} & 0\\ 0 & i\kappa_{1,2} & i(\omega_{r2}-\omega)+\kappa_2 & iG_2\\ 0 & 0 & iG_2 & i(\Omega_{S2}-\omega)+\gamma_2\end{pmatrix}}_{\hat{C}}\begin{pmatrix}\langle c_1\rangle\\ \langle a_1\rangle\\ \langle a_2\rangle\\ \langle c_2\rangle\end{pmatrix}. \quad \text{(D23)}$$

Here, $\kappa_j$ is the overall photon decay rate for $\langle a_j\rangle$ in each LER, $\kappa_{c,j}$ the coupling rate of each LER to the readout transmission line, $\gamma_j$ the total loss rate for each molecular spin, and $\gamma_{c,j}$ accounts for the direct coupling between the spins and the transmission line. Throughout this Appendix, $\gamma_{c,j}$ denotes a real and non-negative rate, while the corresponding coupling amplitude is the complex quantity $\sqrt{\gamma_{c,j}}\,e^{i\phi_j}$. The phase $\phi_j$ is defined relative to that of the LER-line couplings $\sqrt{\kappa_{c,j}}$, which are taken to be real and non-negative. The same complex amplitude, phase included, enters both the drive vector of Eq. (D23) and the output relation, Eq. (D31).

For the present analysis, we neglect the coupling between the spin ensembles and the transmission line (i.e., we make $\gamma_{c,j} = 0$), as the contact between the deposited sample and the line is usually minimal. This simplification enables us to derive an analytical expression for the transmission based on the response of each resonator to the driving field, which is given by

$$S_{21} = 1 - \left( \sqrt{\kappa_{c1}} \frac{i\langle a_1 \rangle}{\alpha_{\text{in}}} + \sqrt{\kappa_{c2}} \frac{i\langle a_2 \rangle}{\alpha_{\text{in}}} \right). \tag{D24}$$

Now $\langle a_1 \rangle$ and $\langle a_2 \rangle$ can be obtained analytically by inverting the $4 \times 4$ matrix on the right-hand side of Eq. (D23). Denoting that matrix by $\hat{C}$ and applying $\hat{C}^{-1}$ to both sides of Eq. (D23), we have (recall we set $\gamma_{c1} = \gamma_{c2} = 0$)

$$\frac{i\langle a_1 \rangle}{\alpha_{\text{in}}} = \left[ \hat{C}^{-1} \begin{pmatrix} 0 \\ \sqrt{\kappa_{c1}} \\ \sqrt{\kappa_{c2}} \\ 0 \end{pmatrix} \right]_2 = (\hat{C}^{-1})_{2,2} \sqrt{\kappa_{c1}} + (\hat{C}^{-1})_{2,3} \sqrt{\kappa_{c2}} \tag{D25}$$

$$\frac{i\langle a_2 \rangle}{\alpha_{\text{in}}} = \left[ \hat{C}^{-1} \begin{pmatrix} 0 \\ \sqrt{\kappa_{c1}} \\ \sqrt{\kappa_{c2}} \\ 0 \end{pmatrix} \right]_3 = (\hat{C}^{-1})_{3,2} \sqrt{\kappa_{c1}} + (\hat{C}^{-1})_{3,3} \sqrt{\kappa_{c2}}, \tag{D26}$$

where we have denoted $[\cdot]_m$ the $m$th component of the corresponding column vector. Thus, we see that we only need four of the matrix elements of $\hat{C}^{-1}$ (three actually, as $\hat{C}$ is symmetric).

In order to get those matrix elements, we write our 3-diagonal symmetric matrix $\hat{C}$ compactly as follows:

$$\hat{C} = \begin{pmatrix} u_1 & v_1 & 0 & 0 \\ v_1 & u_2 & v_2 & 0 \\ 0 & v_2 & u_3 & v_3 \\ 0 & 0 & v_3 & u_4 \end{pmatrix}. \tag{D27}$$

We can get the required matrix elements of $\hat{C}^{-1}$ from the corresponding minors of $\hat{C}$ by the formula $(\hat{C}^{-1})_{j,k} = (-1)^{j+k} M_{k,j}/\det \hat{C}$. Here the minor $M_{j,k}$ is the determinant of the submatrix obtained by deleting the $j$th row and the $k$th column of $\hat{C}$.

All determinants involved can be written in terms of the following two combinations

$$\vartheta_1 = u_1 u_2 - v_1^2$$
$$\vartheta_2 = u_3 u_4 - v_3^2,$$

which are the determinants of the $2 \times 2$ diagonal boxes in which the matrix can be partitioned. Indeed, $\det \hat{C} = \vartheta_1 \vartheta_2 - u_1 u_4 v_2^2$, while

$$(\hat{C}^{-1})_{2,2} = u_1 \vartheta_2 / \det \hat{C}$$
$$(\hat{C}^{-1})_{3,3} = u_4 \vartheta_1 / \det \hat{C}$$
$$(\hat{C}^{-1})_{2,3} = (\hat{C}^{-1})_{3,2} = -(u_1 u_4) v_2 / \det \hat{C}.$$

The last two are duly equal, since $\hat{C}^{-1}$ ought to be symmetric too. The $3 \times 3$ minors employed come out readily, as the matrix has many zeros. As for $\det \hat{C}$, it follows by Laplace expansion as

$$\begin{aligned} \det \hat{C} &= u_1 \begin{vmatrix} u_2 & v_2 & 0 \\ v_2 & u_3 & v_3 \\ 0 & v_3 & u_4 \end{vmatrix} - v_1 \begin{vmatrix} v_1 & 0 & 0 \\ v_2 & u_3 & v_3 \\ 0 & v_3 & u_4 \end{vmatrix} \\ &= u_1 [u_2 \underbrace{(u_3 u_4 - v_3^2)}_{\vartheta_2} - u_4 v_2^2] - v_1^2 \underbrace{(u_3 u_4 - v_3^2)}_{\vartheta_2} \\ &= \underbrace{(u_1 u_2 - v_1^2)}_{\vartheta_1} \vartheta_2 - u_1 u_4 v_2^2. \end{aligned}$$

Let us now plug the above $\hat{C}^{-1}$ matrix elements in the right-hand side of Eqs. (D25) and (D26) and then assemble the term in the parenthesis of Eq. (D24). The result reads

$$\begin{aligned} &\sqrt{\kappa_{c1}} \frac{i\langle a_1 \rangle}{\alpha_{\text{in}}} + \sqrt{\kappa_{c2}} \frac{i\langle a_2 \rangle}{\alpha_{\text{in}}} \\ &\quad = \frac{\kappa_{c1} u_1 \vartheta_2 + \kappa_{c2} u_4 \vartheta_1 - 2\sqrt{\kappa_{c1}\kappa_{c2}}\,(u_1 u_4) v_2}{\vartheta_1 \vartheta_2 - (u_1 u_4) v_2^2}. \end{aligned}$$

Finally, we divide numerator and denominator by $u_1 u_4$, introduce $z_1 \equiv \vartheta_1/u_1 = u_2 - v_1^2/u_1$ and $z_2 \equiv \vartheta_2/u_4 = u_3 - v_3^2/u_4$, so we can write

$$S_{21} = 1 - \frac{\kappa_{c1} z_2(\omega) + \kappa_{c2} z_1(\omega) - 2i\sqrt{\kappa_{c1}\kappa_{c2}}\,\kappa_{1,2}}{z_1(\omega) z_2(\omega) + \kappa_{1,2}^2}. \tag{D28}$$

Here we reverted to the original $-v_1^2 = G_1^2$ and $-v_3^2 = G_2^2$, along with $v_2 = i\kappa_{1,2}$. We close with explicit expressions for the important functions $z_1$ and $z_2$. They can be written in a unified way as ($j = 1, 2$)

$$z_j(\omega) = [i(\omega_{rj} - \omega) + \kappa_j] + \frac{G_j^2}{[i(\Omega_{Sj} - \omega) + \gamma_j]}. \quad \text{(D29)}$$

The terms in the square brackets are $u_2$ and $u_1$, for $j = 1$, and $u_3$ and $u_4$, when $j = 2$, as given in the original matrix. Equipped with these expressions, we can extract the values of the parameters defining our model from the experimental measurements.

### 3. Application

#### a. One spin ensemble scenario: Microwave transmission and remote spin-photon coupling

Analogous to the theoretical framework developed previously, we begin by examining the case where only one LER within a pair couples to a spin ensemble, while the other remains empty. This scenario corresponds to the experiments performed with LER-9 and LER-10, shown in Fig. 3. Microwave transmission results obtained for this system are shown in Fig. 25, which show an effective coupling of the spin ensemble to both cavity modes.

In order to extract the effective coupling constants, we adopt the following strategy. First, we treat the spin-free LER-9 as if it were a standard LER coupled to a spin ensemble with a characteristic coupling constant given by $G_{9,10}$. Using input-output theory in the weak coupling regime [29], we fit the magnetic field dependence of this LER effective linewidth $\tilde{\kappa}_9$ with the expression:

$$\tilde{\kappa}_9 = \kappa_9 + \left[\frac{G_{9,10}^2}{(\Omega_S - \tilde{\omega}_r)^2 + \gamma^2}\right]\gamma. \quad \text{(D30)}$$

The result is shown in Fig. 25(b). The fit allows estimating $G_{9,10}$, as well as the spin resonance linewidth $\gamma$.

Note that, as discussed in Appendix D 1 a above, the resonance does not occur when the polariton frequency crosses $\omega_{r,9}$ but rather $\tilde{\omega}_-$. Consequently, in Eq. (D30), $\tilde{\omega}_r = \tilde{\omega}_-$. Based on the relationship between $\omega_{r,j}$ and $\tilde{\omega}_\pm$ [cf. Eq. (D6)] along with Eq. (D9) for the remote coupling $G_{9,10}$, we can determine the bare resonance frequencies of each LER and $\kappa_{9,10}$. We find $\kappa_{9,10}/2\pi = 6.49$ MHz, $\omega_{r,10}/2\pi = 2.730$ GHz, $\omega_{r,9}/2\pi = 2.720$ GHz, $\gamma/2\pi = 7.3$ MHz. The fits are shown in Fig. 25. It is worth mentioning that without the presence of the spin ensemble in this experiment, determining the cavity parameters $\omega_{r,j}$ and $\kappa_{9,10}$ would have been impossible. Since the transmission experiment probes the coupled normal modes, we would face an underdetermined system of equations, because distinct sets of values for the detuning between bare resonance frequencies and the inter-resonator coupling can yield the same level splitting. In this scenario, the spin serves to fully characterize the coupled photonic system.

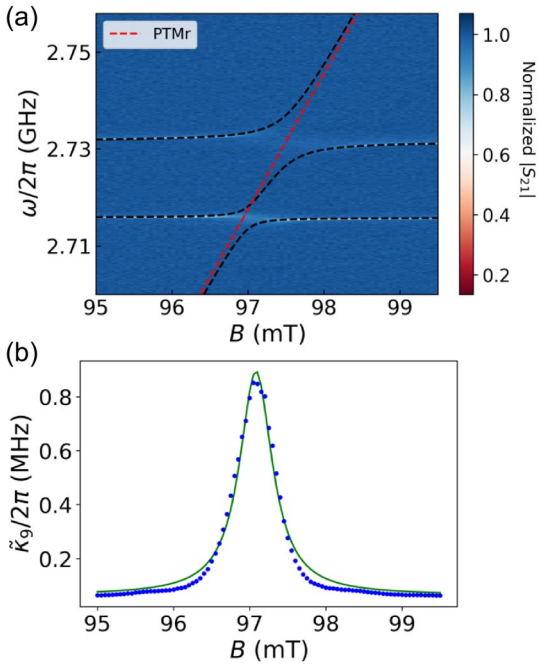


FIG. 25. (a) Result of fitting the eigenvalues of the Hamiltonian (D6) to the experimental modes determined from microwave transmission data for LER-9 and LER-10 (cf. Fig. 3). LER-9 remains empty while LER-10 hosts a PTMr sample, whose resonance frequency is shown as a red dotted line, leading to a local spin-photon collective coupling $G_{10}/2\pi = 5.4$ MHz. (b) Effective half width at half maximum of LER-9 as a function of magnetic field (dots) and least-squares fit based on Eq. (D30), yielding $G_{9,10}/2\pi = 2.46$ MHz.

In order to validate this procedure, we calculate the microwave transmission of two generic LER-1 and LER-2 forming a coupled pair with Eq. (D28) and with all parameters, save for $\kappa_{1,2}$, as given above. By varying $\kappa_{1,2}$, we have checked that the remote coupling $G_{9,10}$ derived from the fits of microwave transmission based on Eq. (D30), follows the expected trend, predicted by (D9). The results, displayed in Fig. 26, confirm that the analysis of the experimental results in Fig. 25 does indeed provide a $G_{9,10}$ value consistent with theory.

Finally, we also test the prediction of Eq. (D12) for the crossing magnetic field between the polariton formed at the LER that hosts a spin ensemble and the normal mode that is closest to the other LER. We consider a LER pair formed by LER-1, strongly coupled to a spin ensemble, and the empty LER-2. Figure 27 shows microwave transmission maps calculated for different values of $\kappa_{1,2}$. In this figure, a yellow star marks the crossing predicted by Eq. (D12), which agrees very well with that estimated from the microwave transmission calculations. These results also confirm that the crossing approaches the

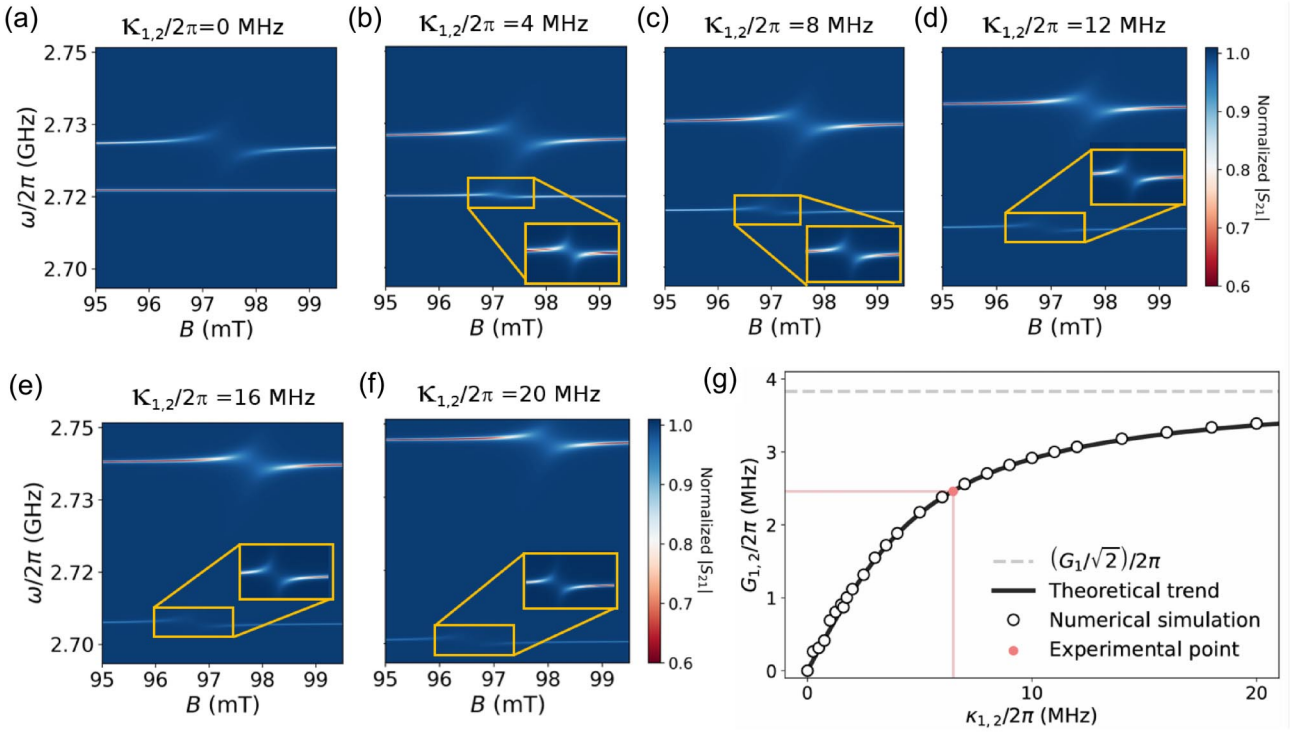


FIG. 26. (a)–(f) 2$D$ microwave transmission maps calculated with Eq. (D28) for a coupled LER-1 and LER-2 pair with different values of $\kappa_{1,2}$, as indicated. The lowest frequency LER-1 remains empty, i.e., $G_1 = 0$, while LER-2 couples to a spin ensemble with $G_2/2\pi = 5.4$ MHz. Other relevant parameters are close to those estimated for LER-9 and LER-10, shown in Fig. 3. As $\kappa_{1,2}$ increases, the avoided level crossing observed for LER-1 widens. (g) Remote coupling of the spin ensemble to LER-1, $G_{1,2}$, determined by fitting the LER-1 resonance with $|S_{21}| = |1 - \frac{\kappa_{e,1}}{z_1(\omega)}|$, where $z_1(\omega) = i(\omega_{r,1} - \omega) + \kappa + \frac{G_{1,2}^2}{i(\Omega_{S,2} - \omega) + \gamma_2}$ [cf. Eq. (D29)]. The solid line follows the prediction given by Eq. (D9). The orange solid dot is the experimental $G_{9,10}$ coupling constant, which allows extracting $\kappa_{1,2}$.

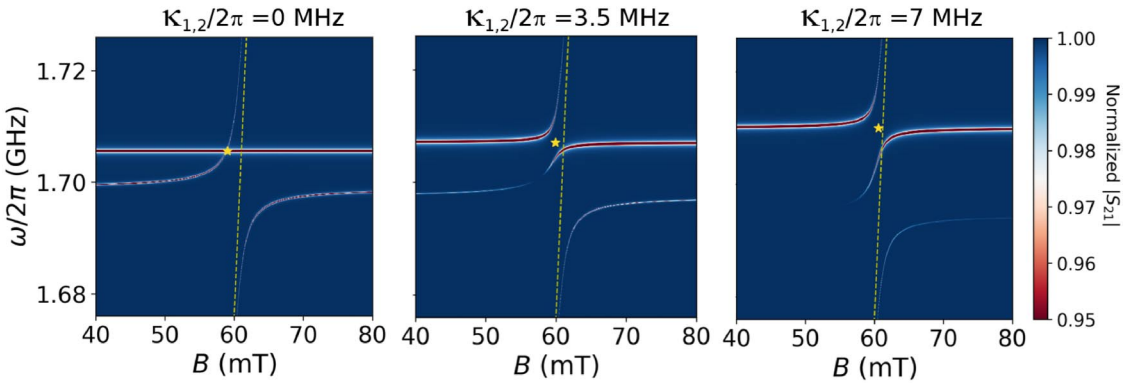


FIG. 27. Transmission signal for a LER pair coupled to one spin ensemble and for different values of $\kappa_{1,2}$, calculated using Eq. (D28). The lower frequency LER-1 interacts with a molecular sample ($G_1/2\pi \approx 20$ MHz) and LER-2 is empty. The yellow dotted line denotes the bare $\Omega_{S,1}$ as a function of magnetic field. The anticrossing occurs at the magnetic field where the frequency of the polariton mode formed at LER-1, not $\Omega_{S,1}$, crosses the frequency of the other normal mode, as predicted by (D12) that is marked by a star.

bare spin resonance (indicated by a yellow dashed line) as $\kappa_{1,2}$ increases.

### b. Two spin ensemble scenario: Eigenstates, microwave transmission and polariton visibilities

We now turn to the case involving two distinct spin ensembles, each coupled to a different LER. Similarly to the previous case, we can extract the relevant parameters in Eq. (D1) by fitting the experimental transmission data. In this way, we are able to determine the local spin-photon couplings ($G_1/2\pi = 19.5$ MHz, and $G_2/2\pi = 8.5$ MHz), the inter-cavity coupling ($\kappa_{1,2}/2\pi = 1.06$ MHz), and the bare LER frequencies ($\omega_{r,1}/2\pi = 1.7029$ GHz and $\omega_{r,2}/2\pi = 1.7096$ GHz). Figure 28 shows that the system

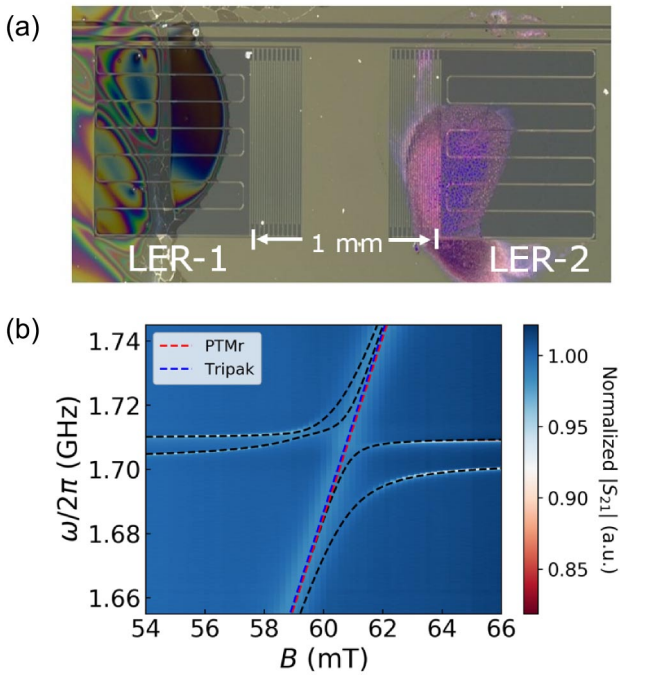


FIG. 28. (a) Optical microscopy image of coupled LER-1 and LER-2, hosting $N \sim 5 \times 10^{14}$ PTMr and Tripak$^{-}$ free radical molecules, respectively. (b) $2D$ microwave transmission map measured at $T = 11$ mK and as a function of magnetic field, near their resonance frequencies. The lines show the eigenfrequencies obtained by exact diagonalization of the Hamiltonian (D1) using the parameter values derived by fitting the experimental transmission with Eq. (D28). We find $\omega_{r,1}/2\pi = 1.703$ GHz, $\omega_{r2}/2\pi = 1.710$ GHz, $G_1/2\pi = 19.5$ MHz, $G_2/2\pi = 8.5$ MHz and $\kappa_{1,2}/2\pi = 1.06$ MHz.

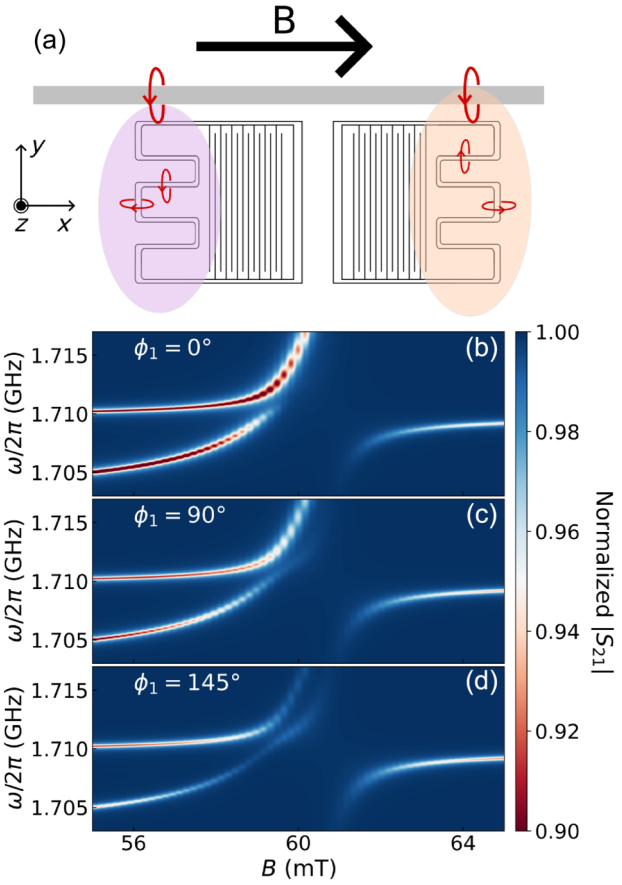


FIG. 29. (a) Sketch of the LER-1 and LER-2 pair, showing the coupling of the Tripak$^{-}$ (purple) and PTMr (orange) molecular spin ensembles to each LER and to the readout transmission line (in gray at the top). (b)–(d) Dependence of microwave transmission visibility on the phase $\phi_1$, i.e., on the effective relative angle between the microwave field generated by the transmission line and the field generated by the LER inductor. The microwave $2D$ map in panel (d) corresponds to the final fit shown in Fig. 5(c).

eigenfrequencies obtained by the exact diagonalization of the Hamiltonian reproduce the experimental modes.

There is, however, an interesting detail concerning the experimental visibilities of some of these modes. Figure 4(f) shows that one of the two polariton branches becomes darker, while the other one becomes brighter near their avoided crossing. Yet, none of them vanishes. This seems at odds with the theoretical predictions derived from Eq. (D28) for this system. If one examines the wave functions obtained numerically for this model, it is observed that the $|\psi_3\rangle$ eigenstate becomes an antisymmetric combination of LER-1 and LER-2 photons near the anticrossing [Figs. 23(c) and 23(e)]. According to Eq. (D24), at the point where this perfectly antisymmetric superposition occurs null visibility is expected. That is, the normalized transmission should reach unity at that point, as we are dealing with a dark state. The nonzero visibility observed experimentally calls for some asymmetry in the coupling of both LERs to the readout line.

In order to properly describe this effect, it is necessary to include in the model a direct coupling between both spin ensembles and the readout waveguide, represented in Eq. (D23) by the parameters $\gamma_{c,j}$. Furthermore, given the microscopic geometry of the system [see Fig. 29(a)], we treat this coupling as a complex number. This additional phase accounts for the fact that spins within the ensemble do not all experience the same microwave magnetic field, differing not only in magnitude (due to varying proximity to the inductor lines) but also in phase (as this particular resonator design exhibits a nonzero field component along any direction). Figure 29 shows that a real coupling amplitude, i.e., $\phi_j = 0$, is insufficient; rather, it is the phase $\phi_1$ that modifies the visibility of the polariton branch of interest. Given the experimental situation, we take $\gamma_{c,1}/2\pi = 65$ kHz together with a finite phase $\phi_1$, and $\gamma_{c,2} = 0$. This change in Eq. (D23) forces to resort to numerical analysis to compute the response for the operators and hence the microwave transmission, which now takes the form

$$S_{21} = 1 - \sqrt{\kappa_{c,1}}\frac{i\langle a_1\rangle}{\alpha_{in}} - \sqrt{\kappa_{c2}}\frac{i\langle a_2\rangle}{\alpha_{in}} - \sqrt{\gamma_{c1}}\,e^{i\phi_1}\frac{i\langle c_1\rangle}{\alpha_{in}}. \tag{D31}$$

This expression qualitatively reproduces the signal shown in Fig. 4. A more refined fit would require accounting for the specific field distribution and orientations derived from the microscopic model.


[1] A. Blais, R.-S. Huang, A. Wallraff, S. M. Girvin, and R. J. Schoelkopf, *Cavity quantum electrodynamics for superconducting electrical circuits: An architecture for quantum computation*, Phys. Rev. A **69**, 062320 (2004).

[2] A. Blais, A. L. Grimsmo, S. M. Girvin, and A. Wallraff, *Circuit quantum electrodynamics*, Rev. Mod. Phys. **93**, 025005 (2021).

[3] A. Wallraff, D. I. Schuster, A. Blais, L. Frunzio, R.-S. Huang, J. Majer, S. Kumar, S. M. Girvin, and R. J. Schoelkopf, *Strong coupling of a single photon to a superconducting qubit using circuit quantum electrodynamics*, Nature (London) **431**, 162 (2004).

[4] T. Niemczyk, F. Deppe, H. Huebl, E. P. Menzel, F. Hocke, M. J. Schwarz, J. J. Garcia-Ripoll, D. Zueco, T. Hümmer, E. Solano, A. Marx, and R. Gross, *Circuit quantum electrodynamics in the ultrastrong-coupling regime*, Nat. Phys. **6**, 772 (2010).

[5] A. Wallraff, D. I. Schuster, A. Blais, L. Frunzio, J. Majer, M. H. Devoret, S. M. Girvin, and R. J. Schoelkopf, *Approaching unit visibility for control of a superconducting qubit with dispersive readout*, Phys. Rev. Lett. **95**, 060501 (2005).

[6] A. A. Houck, D. I. Schuster, J. M. Gambetta, J. A. Schreier, B. R. Johnson, J. M. Chow, L. Frunzio, J. Majer, M. H. Devoret, S. M. Girvin, and R. J. Schoelkopf, *Generating single microwave photons in a circuit*, Nature (London) **449**, 328 (2007).

[7] C. Bonizzoni, A. Ghirri, F. Santanni, M. Atzori, L. Sorace, R. Sessoli, and M. Affronte, *Storage and retrieval of microwave pulses with molecular spin ensembles*, npj Quantum Inf. **6**, 68 (2020).

[8] C. Bonizzoni, A. Ghirri, F. Santanni, and M. Affronte, *Quantum sensing of magnetic fields with molecular spins*, npj Quantum Inf. **10**, 41 (2024).

[9] R. J. Schoelkopf and S. M. Girvin, *Wiring up quantum systems*, Nature (London) **451**, 664 (2008).

[10] J. Majer, J. M. Chow, J. M. Gambetta, J. Koch, B. R. Johnson, J. A. Schreier, L. Frunzio, D. I. Schuster, A. A. Houck, A. Wallraff, A. Blais, M. H. Devoret, S. M. Girvin, and R. J. Schoelkopf, *Coupling superconducting qubits via a cavity bus*, Nature (London) **449**, 443 (2007).

[11] M. Pita-Vidal, J. J. Wesdorp, L. J. Splitthoff, A. Bargerbos, Y. Liu, L. P. Kouwenhoven, and C. K. Andersen, *Strong tunable coupling between two distant superconducting spin qubits*, Nat. Phys. **20**, 1158 (2024).

[12] F. Borjans, X. G. Croot, X. Mi, M. J. Gullans, and J. R. Petta, *Resonant microwave-mediated interactions between distant electron spins*, Nature (London) **577**, 195 (2020).

[13] P. Harvey-Collard, J. Dijkema, G. Zheng, A. Sammak, G. Scappucci, and L. M. K. Vandersypen, *Coherent spin-spin coupling mediated by virtual microwave photons*, Phys. Rev. X **12**, 021026 (2022).

[14] J. Dijkema, X. Xue, P. Harvey-Collard, M. Rimbach-Russ, S. L. de Snoo, G. Zheng, A. Sammak, G. Scappucci, and L. M. K. Vandersypen, *Cavity-mediated iSWAP oscillations between distant spins*, Nat. Phys. **21**, 168 (2025).

[15] R. H. Dicke, *Coherence in spontaneous radiation processes*, Phys. Rev. **93**, 99 (1954).

[16] D. I. Schuster, A. P. Sears, E. Ginossar, L. DiCarlo, L. Frunzio, J. J. L. Morton, H. Wu, G. A. D. Briggs, B. B. Buckley, D. D. Awschalom, and R. J. Schoelkopf, *High-cooperativity coupling of electron-spin ensembles to superconducting cavities*, Phys. Rev. Lett. **105**, 140501 (2010).

[17] Y. Kubo, F. R. Ong, P. Bertet, D. Vion, V. Jacques, D. Zheng, A. Dréau, J.-F. Roch, A. Auffeves, F. Jelezko, J. Wrachtrup, M. F. Barthe, P. Bergonzo, and D. Esteve, *Strong coupling of a spin ensemble to a superconducting resonator*, Phys. Rev. Lett. **105**, 140502 (2010).

[18] H. Wu, R. E. George, J. H. Wesenberg, K. Mølmer, D. I. Schuster, R. J. Schoelkopf, K. M. Itoh, A. Ardavan, J. J. L. Morton, and G. A. D. Briggs, *Storage of multiple coherent microwave excitations in an electron spin ensemble*, Phys. Rev. Lett. **105**, 140503 (2010).

[19] R. Amsüss, C. Koller, T. Nöbauer, S. Putz, S. Rotter, K. Sandner, S. Schneider, M. Schramböck, G. Steinhauser, H. Ritsch, J. Schmiedmayer, and J. Majer, *Cavity QED with magnetically coupled collective spin states*, Phys. Rev. Lett. **107**, 060502 (2011).

[20] S. Probst, H. Rotzinger, S. Wünsch, P. Jung, M. Jerger, M. Siegel, A. V. Ustinov, and P. A. Bushev, *Anisotropic rare-earth spin ensemble strongly coupled to a superconducting resonator*, Phys. Rev. Lett. **110**, 157001 (2013).

[21] A. J. Sigillito, H. Malissa, A. M. Tyryshkin, H. Riemann, N. V. Abrosimov, P. Becker, H.-J. Pohl, M. L. W. Thewalt, K. M. Itoh, J. J. L. Morton, A. A. Houck, D. I. Schuster, and S. A. Lyon, *Fast, low-power manipulation of spin ensembles in superconducting microresonators*, Appl. Phys. Lett. **104**, 222407 (2014).

[22] A. Ghirri, C. Bonizzoni, D. Gerace, S. Sanna, A. Cassinese, and M. Affronte, $YBa_2Cu_3O_7$ *microwave resonators for strong collective coupling with spin ensembles*, Appl. Phys. Lett. **106**, 184101 (2015).

[23] A. Bienfait, A. A. Pla, Y. Kubo, X. Stern, C. C. Lo, C. D. Weis, T. Schenkel, M. L. W. Thewalt, D. Vion, D. Esteve, B. Julsgaard, K. Mølmer, J. J. L. Morton, and P. Bertet, *Reaching the quantum limit of sensitivity in electron spin resonance*, Nat. Nanotech. **11**, 253 (2016).

[24] C. Eichler, A. J. Sigillito, S. A. Lyon, and J. R. Petta, *Electron spin resonance at the level of* $10^4$ *spins using low impedance superconducting resonators*, Phys. Rev. Lett. **118**, 037701 (2017).

[25] S. Probst, A. Bienfait, P. Campagne-Ibarcq, J. J. Pla, B. Albanese, J. F. Da Silva Barbosa, T. Schenkel, D. Vion, D. Esteve, K. Mølmer, J. J. L. Morton, R. Heeres, and P. Bertet, *Inductive-detection electron-spin resonance spectroscopy with 65 spins/Hz sensitivity*, Appl. Phys. Lett. **111**, 202604 (2017).

[26] C. Bonizzoni, A. Ghirri, M. Atzori, L. Sorace, R. Sessoli, and A. Affronte, *Coherent coupling between Vanadyl Phthalocyanine spin ensemble and microwave photons: towards integration of molecular spin qubits into quantum circuits*, Sci. Rep. **7**, 13096 (2017).

[27] M. Mergenthaler, J. Liu, J. J. Le Roy, N. Ares, A. L. Thompson, L. Bogani, F. Luis, S. J. Blundell, T. Lancaster, A. Ardavan, G. A. D. Briggs, P. J. Leek, and E. A. Laird, *Strong coupling of microwave photons to antiferromagnetic fluctuations in an organic magnet*, Phys. Rev. Lett. **119**, 147701 (2017).

[28] S. Lenz, D. König, D. Hunger, and J. van Slageren, *Room-temperature quantum memories based on molecular electron spin ensembles*, Adv. Mater. **33**, 2101673 (2021).

[29] V. Rollano, M. C. de Ory, C. D. Buch, M. Rubín-Osanz, D. Zueco, C. Sánchez-Azqueta, A. Chiesa, D. Granados, S. Carretta, A. Gomez, S. Piligkos, and F. Luis, *High cooperativity coupling to nuclear spins on a circuit quantum electrodynamics architecture*, Commun. Phys. **5**, 246 (2022).

[30] M. Rubín-Osanz, M. C. de Ory, I. Gimeno, D. Granados, D. Zueco, A. Gomez, and F. Luis, *Coupling organic free-radical molecules to lumped-element superconducting resonators*, Low Temp. Phys. **50**, 472 (2024).

[31] Y. Mao, H.-Y. Ren, Z.-Y. Liu, Y.-Z. Zhen, T. Rong, T. Jiang, Z. Chen, Z.-H. Yuan, W.-H. Qin, X. Zhang, X. Liu, M. Gong, K. Nemoto, W. J. Munro, and J. Majer, *Strong coupling in a three-mode superconducting-spin hybrid quantum system*, Phys. Rev. Res. **8**, 023343 (2026).

[32] T. Astner, S. Nevlacsil, N. Peterschofsky, A. Angerer, S. Rotter, S. Putz, J. Schmiedmayer, and J. Majer, *Coherent coupling of remote spin ensembles via a cavity bus*, Phys. Rev. Lett. **118**, 140502 (2017).

[33] A. Ghirri, C. Bonizzoni, F. Troiani, N. Buccheri, L. Beverina, A. Cassinese, and M. Affronte, *Coherently coupling distinct spin ensembles through a high-$T_c$ superconducting resonator*, Phys. Rev. A **93**, 063855 (2016).

[34] E. Moreno-Pineda, C. Godfrin, F. Balestro, W. Wernsdorfer, and M. Ruben, *Molecular spin qudits for quantum algorithms*, Chem. Soc. Rev. **47**, 501 (2018).

[35] M. Atzori and R. Sessoli, *The second quantum revolution: Role and challenges of molecular chemistry*, J. Am. Chem. Soc. **141**, 11339 (2019).

[36] A. Gaita-Ariño, F. Luis, S. Hill, and E. Coronado, *Molecular spins for quantum computation*, Nat. Chem. **11**, 301 (2019).

[37] S. Carretta, D. Zueco, A. Chiesa, Á Gómez-León, and F. Luis, *A perspective on scaling up quantum computation with molecular spins*, Appl. Phys. Lett. **118**, 240501 (2021).

[38] A. A. Fursina and A. Sinitskii, *Toward molecular spin qubit devices: Integration of magnetic molecules into solid-state devices*, ACS Appl. Electron. Mater. **5**, 3531 (2023).

[39] A. Chiesa, P. Santini, E. Garlatti, F. Luis, and S. Carretta, *Molecular nanomagnets: A viable path toward quantum information processing?*, Rep. Prog. Phys. **87**, 034501 (2024).

[40] E. Moreno-Pineda and W. Wernsdorfer, *Magnetic molecules as building blocks for quantum technologies*, Adv Quantum Technol. **8**, 2300367 (2025).

[41] A. Chiesa, P. Santini, D. Gerace, J. Raftery, A. A. Houck, and S. Carretta, *Digital quantum simulators in a scalable architecture of hybrid spin-photon qubits*, Sci. Rep. **5**, 16036 (2015).

[42] S. Chicco, G. Allodi, A. Chiesa, E. Garlatti, C. D. Buch, P. Santini, R. De Renzi, S. Piligkos, and S. Carretta, *Proof-of-concept quantum simulator based on molecular spin qudits*, J. Am. Chem. Soc. **146**, 1053 (2024).

[43] S. Roca-Jerat, E. Macaluso, A. Chiesa, P. Santini, and S. Carretta, *Simulating open quantum systems with molecular spin qudits*, Mater. Horiz. **12**, 3918 (2025).

[44] M. D. Jenkins, D. Zueco, O. Roubeau, G. Aromí, J. Majer, and F. Luis, *A scalable architecture for quantum computation with molecular nanomagnets*, Dalton Trans. **45**, 16682 (2016).

[45] A. Chiesa, S. Roca, S. Chicco, M. C. de Ory, A. Gómez-León, A. Gomez, D. Zueco, F. Luis, and S. Carretta, *Blueprint for a molecular-spin quantum processor*, Phys. Rev. Appl. **19**, 064060 (2023).

[46] O. Noroozian, P. K. Day, B. H. Eom, H. G. Leduc, and J. Zmuidzinas, *Crosstalk reduction for superconducting microwave resonator arrays*, IEEE Trans. Microwave Theory Tech. **60**, 1235 (2012).

[47] P. Pakulski, M. Magott, S. Chorazy, M. Sarewicz, M. Srebro-Hooper, D. Tabor, L. Lapok, D. Szczepanik, S. Demir, and D. Pinkowicz, *A multifunctional pseudo-[6]oxocarbon molecule innate to six accessible oxidation states*, Chem **10**, 971 (2024).

[48] D. Schäfter, J. Wischnat, L. Tesi, J. A. De Sousa, E. Little, J. McGuire, M. Mas-Torrent, C. Rovira, J. Veciana, F. Tuna, N. Crivillers, and J. van Slageren, *Molecular one- and two-qubit systems with very long coherence times*, Adv. Mater. **35**, 2302114 (2023).

[49] O. Armet, J. Veciana, C. Rovira, J. Riera, J. Castaner, E. Molins, J. Rius, C. Miravitlles, S. Olivella, and J. Brichfeus, *Inert carbon free radicals. 8. Polychlorotriphenylmethyl radicals: Synthesis, structure, and spin-density distribution*, J. Phys. Chem. **91**, 5608 (1987).

[50] I. Gimeno, V. Rollano, D. Zueco, Y. Duan, M. C. de Ory, A. Gomez, A. Gaita-Ariño, C. Sánchez-Azqueta, T. Astner, D. Granados, S. Hill, J. Majer, E. Coronado, and F. Luis, *Optimal coupling of* $HoW_{10}$ *molecular magnets to superconducting circuits near spin clock transitions*, Phys. Rev. Appl. **20**, 044070 (2023).

[51] S. Roca-Jerat, M. Rubín-Osanz, M. D. Jenkins, A. Camón, P. J. Alonso, D. Zueco, and F. Luis, *Waveguide quantum electrodynamics at the onset of spin-spin correlations*, Commun. Mater. **6**, 172 (2025).

[52] M. Mariantoni, F. Deppe, A. Marx, R. Gross, F. K. Wilhelm, and E. Solano, *Two-resonator circuit quantum electrodynamics: A superconducting quantum switch*, Phys. Rev. B **78**, 104508 (2008).

[53] M. Rubín-Osanz *et al.*, *Optimizing magnetic coupling in lumped element superconducting resonators for molecular spin qubits*, arXiv:2511.00857.

[54] M. D. Jenkins, Y. Duan, B. Diosdado, J. J. García-Ripoll, A. Gaita-Ariño, C. Giménez-Saiz, P. J. Alonso, E. Coronado, and F. Luis, *Coherent manipulation of three-qubit states in a molecular single-ion magnet*, Phys. Rev. B **95**, 064423 (2017).

[55] C. Godfrin, A. Ferhat, R. Ballou, S. Klyatskaya, M. Ruben, W. Wernsdorfer, and F. Balestro, *Operating quantum states in single magnetic molecules: implementation of Grover's quantum algorithm*, Phys. Rev. Lett. **119**, 187702 (2017).

[56] H. Biard, E. Moreno-Pineda, M. Ruben, E. Bonet, W. Wernsdorfer, and F. Balestro, *Increasing the Hilbert space dimension using a single coupled molecular spin*, Nat. Commun. **12**, 4443 (2021).

[57] M. Rubín-Osanz, L. Bersani, S. Chicco, G. Allodi, R. De Renzi, A. Mavromagoulos, M. D. Roy, S. Piligkos, E. Garlatti, and S. Carretta, *Implementing the Quantum Fourier Transform on a molecular qudit with full refocusing and state tomography*, Nat. Commun. **17**, 6217 (2026).

[58] M. D. Jenkins, T. Hümmer, M. J. Martínez-Pérez, J. J. García-Ripoll, D. Zueco, and F. Luis, *Coupling single-molecule magnets to quantum circuits*, New J. Phys. **15**, 095007 (2013).

[59] A. Pscherer, J. Liersch, P. Abgrall, A. D. Beyer, F. Defrance, S. R. Gowala, H. L. Sueur, J. O'Sullivan, E. Flurin, and P. Bertet, *Superconducting parallel-plate resonators for the detection of single electron spins*, arXiv:2603.25258.

[60] N. T. Bronn, Y. Liu, J. B. Hertzberg, A. D. Córcoles, A. A. Houck, J. M. Gambetta, and J. M. Chow, *Broadband filters for abatement of spontaneous emission in circuit quantum electrodynamics*, Appl. Phys. Lett. **107**, 172601 (2015).

[61] C. del Rio, S. Roca-Jerat, and F. Luis Vitalla, *Polariton-polariton coherent coupling in a molecular spin-superconductor chip-dataset*, Zenodo (2026), https://zenodo.org/records/23739959.

[62] H. R. Mohebbi, O. W. B. Benningshof, I. A. J. Taminiau, G. X. Miao, and D. G. Cory, *Composite arrays of superconducting microstrip line resonators*, J. Appl. Phys. **115**, 094502 (2014).

[63] Sonnet Software, Inc., *Sonnet User's Guide, Version 18* (Sonnet Software, Inc., New York, 2024).

[64] R. Manenti and M. Motta, *Quantum Information Science* (Oxford University Press, Oxford, 2023).

[65] E. T. Jaynes and F. W. Cummings, *Comparison of quantum and semiclassical radiation theories with application to the beam mase*, Proc. IEEE **51**, 89 (1963).

[66] M. Tavis and F. W. Cummings, *Exact solution for an N-molecule—radiation-field Hamiltonian*, Phys. Rev. **170**, 379 (1968).

[67] G. Vidal and R. F. Werner, *Computable measure of entanglement*, Phys. Rev. A **65**, 032314 (2002).

[68] J. R. Schrieffer and P. A. Wolff, *Relation between the Anderson and Kondo Hamiltonians*, Phys. Rev. **149**, 491 (1966).

[69] C. Gardiner and P. Zoller, *Quantum Noise: A Handbook of Markovian and Non-Markovian Quantum Stochastic Methods with Applications to Quantum Optics* (Springer Science & Business Media, Berlin and Heidelberg, 2004).

[70] T. Holstein and H. Primakoff, *Field dependence of the intrinsic domain magnetization of a ferromagnet*, Phys. Rev. **58**, 1098 (1940).